

# Inversion of Broad-Band Multitone Acoustic Data from the YELLOW SHARK Summer Experiments

Jean-Pierre Hermand and Peter Gerstoft

**Abstract**—Integral geoacoustic properties of the sea bottom were determined from full-field inversion of broad-band, waterborne, acoustic propagation data. The data were obtained during the YELLOW SHARK 94 experiment along a 15-km mildly range-dependent transect at a shallow water site in the western Mediterranean. Seven tones from 200 Hz to 800 Hz were transmitted simultaneously by a mid-depth acoustic projector, bottom-moored at different ranges from a vertical array that spanned the water column below the thermocline. Extensive oceanographic and geophysical information were obtained *in situ* to support and validate the inversion. Matched-field processing was applied to the received pressure fields for each tone frequency. Optimization of the environmental parameters was performed simultaneously across all propagated frequencies. A maximum-likelihood objective function included the linear (Bartlett) cross correlator at the individual frequencies. Genetic algorithms searched for the global minimum of this objective function. The convergence and accuracy of the inversion were determined from statistical analysis of the *a posteriori* distribution of the candidate environmental models produced by the search algorithm. The following conclusions were drawn from this study. 1) For a fixed source-vertical array configuration broad-band tomographic measurements were a *sine qua non* to obtain meaningful inversion results. 2) The broad-band inversion provided considerable stability and robustness with respect to volume and bottom variabilities. 3) Corresponding single-frequency inversions performed under the exact same conditions produced erratic results. 4) Integral geoacoustic properties of the bottom were effectively determined within the constraints imposed by the bottom parameterization. 5) More detailed and accurate properties were obtained by including the range dependence of ocean sound-speed profile in the forward modeling. 6) The broad-band-inverted sound-speed profile, attenuation, density, and thickness of the top clay layer, and sound speed of the underlying silt layer, were in close agreement with the independent geophysical measurements.

## I. INTRODUCTION

**B**ROAD-BAND inversion experiments YELLOW SHARK were performed in a shallow water area south of Elba island, off the west coast of Italy, during the summer of 1994 (YS94) and the spring of 1995 (YS95) [1]. The YS95 configuration is depicted in Fig. 1. Comprehensive, high-quality broad-band-acoustic propagation, geophysical and oceanographical data were obtained for the development and validation of broad-band inversion methodologies applicable to the shallow water environment. The key question is: Can we determine *representative* integral environmental properties of

the shallow water medium from the inversion of waterborne acoustic propagation data?

Tomographic inversion infers from the measurement of acoustic properties a model of the environment transversed by the sound field. An important attribute of tomographic measurements is that they are spatially integrating so that integral properties of the environment can be derived within the limits imposed by the propagation medium variabilities and uncertainties. The design of measurement techniques and inversion methods for shallow water tomography must take into account the bottom variability in depth and range to be encountered in a particular environment and need also to consider the ocean volume variability in time and space characterizing this type of environment. The parameterization of the forward problem is of fundamental importance in obtaining unique and robust estimates of the investigated environment. Physical knowledge and *a priori* information should be systematically exploited to eliminate from the inverse problem the need to infer volume and bottom structures, and experimental geometries that are known or directly measurable.

In the deep ocean, the inversion has been based largely upon the acoustic travel times of identifiable multipaths [2]. This method is not applicable to the shallow-water channel due to complex propagation effects incurred by boundary interaction. Inversion in shallow water requires the measurement of acoustic properties that are specific to the waveguide regime. The most promising inversion methods exploit acoustic amplitude and phase information in space and/or time received on hydrophone arrays. The environmental information is obtained by applying optimization techniques to determine the best match between predicted and observed acoustic fields and/or waveforms.

Characterizing a *fading time-dispersive* waveguide with a single-frequency or narrow-band measurement with fixed experimental geometries is somewhat paradoxical and leads to problems of resolution, uniqueness and robustness already encountered in matched-field source localization applications [3]. It is well established that propagation in a shallow water channel is frequency-dependent and sensitive to the boundary conditions. Water depth and in-water sound-speed structure determine how the propagated energy interacts with the ocean boundaries. In particular, the time dispersion characteristics are intrinsically related to the frequency-dependent geoacoustic properties of the sea bottom. Probing the propagation channel over a sufficiently wide band of temporal frequencies will *resolve* both large-scale and small-scale features in the ocean volume and bottom that affect acoustic propagation.

Manuscript received May 1996; revised June 1996.

The authors are with SACLANT Undersea Research Centre, Environmental Research Div., viale San Bartolomeo, 400, I-19138 La Spezia, Italy.

Publisher Item Identifier S 0364-9059(96)07990-3.

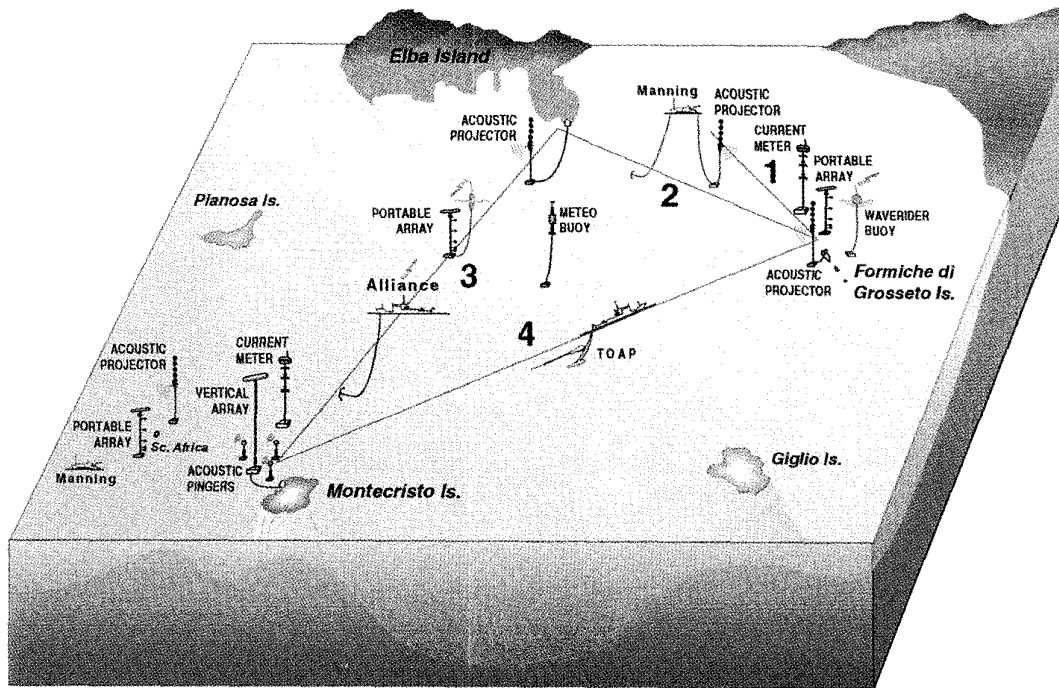


Fig. 1. Configuration of the YELLOW SHARK broad-band inversion experiments in the Giglio basin, off the west coast of Italy. Acoustic tomography instruments were bottom-moored near three islands and at several positions along four transects. The oceanographic phenomena were acoustically monitored in real time during 12 days by 1-min repeated transmissions of broad-band signals in the frequency band 200 Hz–1.6 kHz. The ocean sound-speed structure and sound field across the tomographic sections were measured simultaneously with the acoustic transmissions by a towed oceanographic and acoustic profiler. The geoacoustic properties of the sea bottom along the transects were determined from acoustic stratigraphy, sediment cores, and bottom reflectivity measurements. The distances are 15 km for line 1, and  $40 \times 41 \times 55$  km for triangle 2–3–4.

The closely related problems of source localization and environmental inversion have been addressed principally with narrow-band approaches. Since the work of Bucker [4] the methodologies have been based primarily on matched-field processing (MFP). The majority of MFP research involves the matching of measured and predicted fields at a single frequency. In its original formulation MFP does not take advantage of frequency-dependent propagation effects. As a consequence, when applied to the inverse problem, the method lacks the sensitivity to characterize the shallow-water waveguide, a dispersive medium.

Since the late 1980's, several broad-band approaches for source localization application have been developed and demonstrated experimentally. Following the early work of Parvulescu [5], Clay [6] and Li and Clay [7] have examined time-domain methods for optimum signal transmission and source localization. Bageroer *et al.* [8] investigated numerically incoherent averaging of single-frequency MFP results to reduce localization ambiguities. Westwood [9] developed a broad-band MFP algorithm that involves correlating modeled and measured cross spectra and summing coherently over frequency and hydrophone pairs. Improved localization of a broad-band (55–95 Hz) source towed past a vertical array in the deep ocean was achieved. Hermand and Roderick [10]–[12] demonstrated that the distortion of time-dispersed wide-band (240–740 Hz) signals can be effectively compensated for by using a model-based matched

filter (MBMF) receiver that incorporates a predicted Green's function of the medium. In ducted propagation experiments, a multichannel MBMF receiver determined unambiguously and accurately the range and depth of the towed source emitting the acoustic signal, the depth of the receiving towed array, and their relative velocity. Mignerey and Finette [13] developed and applied a normal-mode Green's function approach to deconvolve the source function (38–50 Hz) and determine its position in a deep ocean experiment. Lu *et al.* [14] developed a time-domain matched-mode processing scheme that separates the range and depth estimation tasks. Jesus [15] applied weighted averaging of narrow-band range-depth ambiguity estimates and obtained stable and accurate localization results for a transient (230–270 Hz) source in a shallow-water experiment. Brienzo and Hodgkiss [16] successfully applied a generalized beamformer to explosive signals (<100 Hz) received on a vertical array in the deep ocean. Yang [17] and Chen and Lu [18] investigated numerically incoherent and coherent matched-mode processing in the time-frequency domain. Related Soviet works were reviewed in [11].

The literature specifically relating to broad-band approaches for environmental inversion application is limited as indicated by the review of the state of the art in [19] and more recent underwater acoustics publications. While there is a considerable interest in the subject, very few experimental works have been reported to date. Since the early work of Pekeris [20], broad-band acoustics have long been used to infer

ocean environmental parameters. Early comparisons of model prediction with broad-band measurement were based largely on transmission loss (TL) [21]. Rubano [22] measured group-velocity dispersion, mode shapes and TL in one-third octave bands ( $<1$  kHz) using explosive charges launched at different ranges from a vertical array. A three-layer bottom model was obtained by iterating a normal-mode model to fit the broad-band acoustic properties. Brown [23] compared linearized inversion schemes to solve for the sound-speed profile (SSP) in the upper kilometer of a range-independent ocean model. Full-waveform and intensity inversions performed significantly better than travel-time inversion when the individual ray arrivals were not resolved. Zhou [24], [25] developed inverse techniques for bottom geoaoustic parameters based on dispersion analysis and normal mode measurements (80–800 Hz) with an experimental setup similar to Rubano's. Rajan, Lynch and Frisk [26], [27] exploited group-velocity curves to invert for bottom geoaoustic properties, and compared narrow-band and broad-band (20–120 Hz) results obtained with linear perturbative inverse techniques. For their synthetic-aperture experimental configuration it was concluded that the narrow-band inverse was as good as the broad-band inverse obtained from Rubano's data.

Recently, Badiey *et al.* [28] conducted a thorough study of the influence of sediment variability on broad-band acoustic wave propagation at a shallow water site, well-documented by geological and geoaoustical data. Hermand and Soukup [29] compared measured and predicted broad-band (200–800 Hz) transfer functions at five ranges along the 40-km tomographic transect 2 in Fig. 1. Beyond the bottom topography, modeling of the *range-dependent* geoaoustic properties was essential to match the measurements at all ranges and frequencies.

In full-field formulations of the shallow-water inverse problem, the relationships between measured acoustic properties and environmental parameters are nonlinear and the resulting objective functions are complex. To circumvent the complexity and lack of flexibility associated with nonlinear optimization techniques, combinatorial methods such as simulated annealing [30] and genetic algorithms (GA) [31] have been considered to minimize the objective function. Gerstoft [32] applied GA to the inversion for geoaoustic parameters and obtained successful results with single-frequency synthetic data. Recently, a GA-based inversion approach was tested with narrow-band array data (170 Hz and 330 Hz) obtained north of Elba island [33]. The objective function consisted of summed powers from the linear (Bartlett) processor at three frequencies spaced by approximately 2 Hz in each band.

In a previous paper [34], Hermand investigated numerically phase-coherent processing in time (MBMF) for the inversion of a summertime shallow-water channel in the YELLOW SHARK experimental area. Wave propagation effects over a broad *continuum* of temporal frequencies were fully integrated into a multimode MBMF receiver by means of predicted broad-band modal responses of the waveguide. In contrast to conventional MFP, the characteristics of the received broad-band modal structure in time and frequency were exploited to infer environmental parameters. This did not require a large multielement vertical array.

In this paper, we investigate a different broad-band approach that entails the *simultaneous* matching of measured and predicted continuous-wave (CW) pressure fields over a wide band of discrete frequencies (200–800 Hz). For inversion purposes, a broad-band MFP (BMFP) approach is analogous to multimode MBMF processing in that MBMF is a coherent process in the time domain over a full band of frequencies *versus* BMFP, which is a coherent process in the spatial domain at a number of frequencies. The BMFP inversion does not require coherency across the narrow frequency bands of the multitone signal. It is emphasized that the inversion method performs a joint optimization across frequencies that is not fully equivalent to the "frequency averaging to reduce ambiguities" as applied to enhance MFP source localization. The inversion will be referred to as "broad-band" even though it is not based on a broad *continuum* of frequencies as for the MBMF.

The method is applied to the inversion of multitone pressure fields measured across the 15 km  $\times$  113 m tomographic section northwest of Formiche di Grosseto islands during YS94 experiment (transect 1 in Fig. 1). The acoustic data consist of seven tones from 200 Hz to 800 Hz transmitted simultaneously from a mid-depth acoustic projector bottom-moored at four ranges to a 62-m vertical receiving array. The propagation conditions were determined by a low-speed, top sediment layer, overlying higher speed layers, and a strongly downward refracting, ocean SSP that maximized bottom interaction. This phase of the investigation focused on the determination of SSP, attenuation, and layer thickness in the sea bottom using extensive hydrographic data obtained during the tomographic measurements.

The present work features 1) *simultaneous* CW pressure-field observations over the broad frequency band 200 Hz–800 Hz, 2) *joint* optimization across all propagated frequencies, 3) measurement at different ranges, 4) accurately known geometries for which inversion is not performed, 5) volume information with full coverage in time and range exploited in the inversion process, 6) comparison of two different parameterizations of the environment to be inverted, 7) validation of the inversion results with independent characterization of the sea bottom, and 8) detailed statistical analysis of a *posteriori* distributions produced by the GA. Points 1), 2), 4), and 8) distinguish this work from previous works.

In Section II, the selected YS94 broad-band-acoustic/environmental data set is discussed with relevant experimental details. A baseline model of the environment is constructed from *in situ* hydrographical and geophysical measurements. In Section III the implementation of broad-band MFP and genetic-algorithms inversion is discussed. In particular, a generalized, maximum-likelihood, objective function is derived. Empirical and data-oriented environmental models are defined for inversion. In Section IV, the inversion of the two bottom models is discussed in detail with emphasis on resolution, uniqueness and robustness. Broad-band inversion results are compared with corresponding single-frequency results and validated with the baseline model. Section V concludes the paper.

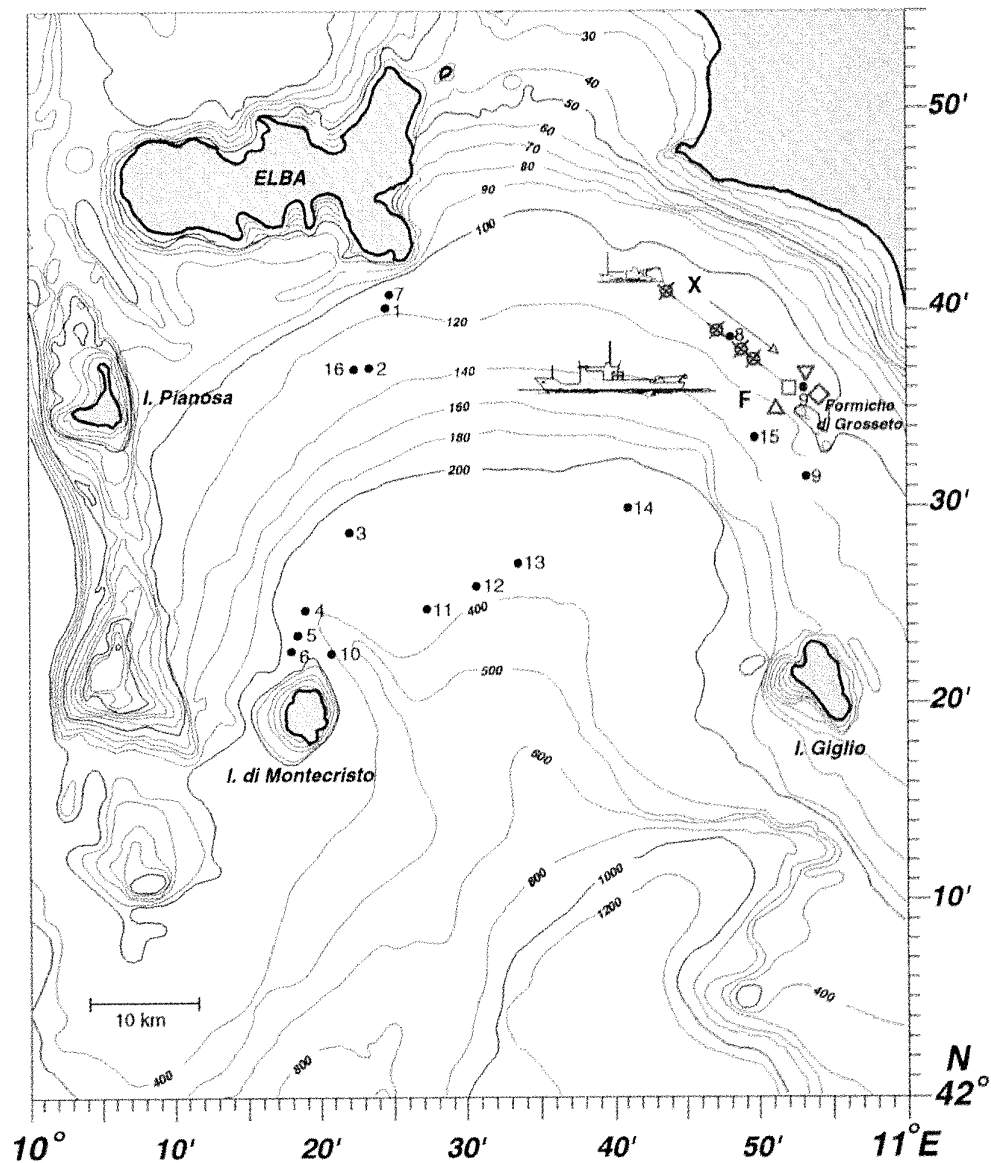


Fig. 2. Map of the YELLOW SHARK 94 experimental configuration. The moorings, northwest of Formiche di Grosseto islands, are located with the following symbols.  $\otimes$ : sound source.  $\square$ : vertical array.  $\diamond$ : waverider buoy.  $\triangle$ : currentmeter chain.  $\nabla$ : meteo buoy. Coring locations are numbered and marked by a  $\bullet$  symbol.

#### A. YS94 Experimental Configuration

A map of the area in Fig. 2 indicates the location of the acoustic and oceanographic moorings deployed during the YELLOW SHARK 94 (YS94) experimental phase. Acoustic signals were transmitted from a sound source deployed by R/V *Manning* successively at four points (X). The signals were received on a vertical array deployed north of Formiche di Grosseto islands in 112-m water depth (F).

Fig. 3 shows the experimental geometry for the acoustic runs considered in this paper. The vertical array was configured with 32 elements equispaced 2 m that spanned the 37–99-m water depths; the 62-m acoustic aperture covered most of the water column below the end-summer thermocline. The

array depth was determined by the preset cable length from the bottom. The array tilt was inferred from current data obtained with a current-meter chain that was bottom-moored near the array. No significant array tilt or shape variation were observed during the acoustic measurements; the magnitude of the water currents near the array at 32-m and 91-m water depths never exceeded 15 cm/s and 7 cm/s, respectively. Measurements of array element positions were also made with three transponders near the mooring as illustrated in Fig. 1. The array was connected with a 2-km cable to the shore.

The sound source was bottom-moored and suspended at 68-m water depth by means of subsurface buoys to eliminate wavefield variation caused by current-induced motion.

The source consisted of two flextensional acoustic projectors covering the frequency bands 200–800 Hz (LF) and 800 Hz–1.6 kHz (HF). The transmitted waveforms were measured in water by a pole-mounted hydrophone in the far field of the source. The waveforms recorded from the reference hydrophone were used to monitor the sound pressure level and to correct for the projector distortions. In this manner, the acoustic measurements were accurately calibrated. The source depth was determined by the preset cable length from the bottom and controlled from a pressure gauge attached to the structure. The source and hydrophone were cable-connected to the driving amplifiers and signal generator, and recording unit installed on board the ship.

Differential global positioning system (DGPS) instruments were used to determine the position of the acoustic moorings to the requisite precision of a few meters; the resulting ranges are indicated in Table II.

### B. Acoustic Transmissions

Each transmitted sequence consisted of a large time-bandwidth (TB) product frequency-modulated waveform followed by a multitone waveform after a dead time. The duration of both waveforms and the dead period were 12 s; the overall pulse repetition rate was 2 min. At each range, the transmissions were performed successively for each frequency band and lasted for 1–2.5 h (Table I).

The large TB-product signals were designed to apply the multimode model-matched filter processing described in [34]. The multitone signals were designed for the broad-band matched-field processing described in Section IV. The multitone signals had third-octave frequencies covering the same frequency band as the broad-band-coded waveforms. The frequencies were 200, 250, 315, 400, 500, 630, and 800 Hz for the LF band, and 800, 1000, 1250, and 1600 Hz for the HF band. The CW components of the LF and HF signals were weighted in amplitude to equalize the transmitting sensitivity response of the respective high- $Q$  flextensional projectors. Only the LF-band multitone data are treated in this paper.

## II. BROAD-BAND INVERSION EXPERIMENTS

During the YELLOW SHARK 94 and 95 experiments over  $10^5$  broad-band-coded signals and 48 h of multitone signals in the frequency band 200 Hz–1.6 kHz were propagated between fixed sound sources and receiving vertical arrays along four transects in the Giglio basin off the west coast of Italy. In this paper, we consider an acoustic/environmental data set obtained on the 10 and 11 September 1994, northwest of Formiche di Grosseto islands where probing signals were propagated for different ranges along the 15-km mildly range-dependent transect 1 (Fig. 1). Environmental information and experimental details related to the analyzed data set are provided.

### C. Shallow Water Variability

The hydrographical conditions were monitored using both satellite remote sensing and *in situ* measurements. Surface thermal images combined with *in situ* temperature, salinity,

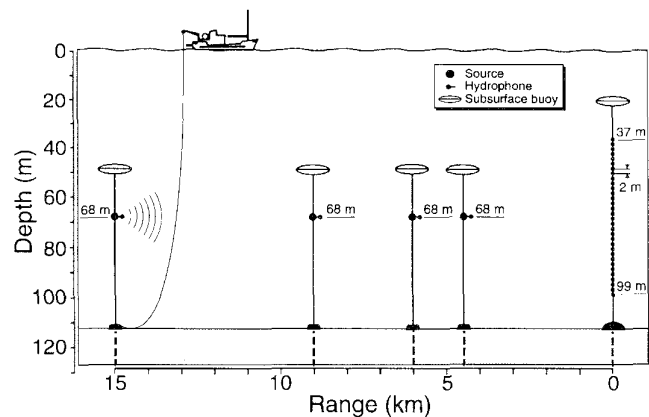


Fig. 3. Geometry for the acoustic transmissions along the YS94 transect northwest of Formiche di Grosseto islands. On 10 September 1994, the sound source was deployed at 15 km and 9 km ranges from the fixed receiving array, and on 11 September, at 6 km and 4.5 km ranges.

TABLE I  
ACOUSTIC DATA RECORDING PERIODS

Day	Time (h UTC)	Range (km)	Frequency band (Hz)	Number of signals
10 Sept 94	1012–1242	15	200–800	71
	1256–1526		800–1600	71
	1740–1948	9	200–800	49
	2016–2158		800–1600	50
11 Sept 94	0720–0820	6	200–800	31
	0834–0932		800–1600	29
	1202–1304	4.5	800–1600	32
	1318–1418		200–800	31

Related environmental data can be obtained from [35].

TABLE II  
EXPERIMENTAL GEOMETRIES, MIXED-LAYER THICKNESS, WATER DEPTH, AND TOP-LAYER THICKNESS VARIABILITIES

Range (m)	Source depth (m)	Receiver depth (m)	Mixed layer thickness (m)	Water depth (m)	Top layer thickness (m)
15021	87.7	37.2–99.2	19.6±0.9	113.4±0.8	6.9±1.0
9026	69.2	37.2–99.2	18.8±0.7	113.1±0.7	7.4±0.9
6087	69.0	37.2–99.2	20.8±1.1	112.9±0.7	8.0±0.6
4524	68.6	37.2–99.2	22.0±0.8	112.5±0.5	8.1±0.5

In the last three columns, mean and one standard deviation values along the transect are given. The mixed-layer thickness is taken as the depth at which the temperature decreases by more than 0.1 °C.

and current observations provided a synoptic view of the hydrographical conditions during the acoustic transmissions.

1) *Sea Surface Temperature*: Infrared satellite remote sensing provided on clear-sky days the sea surface thermal structure over the experimental area [36]. Meteorological data were acquired by the ship-borne meteo station. Surface roughness and wave spectra were obtained from a waverider buoy deployed near the receiving array.

Fig. 4 shows the sea-surface temperature (SST) in the afternoons on the 10 and 11 September 1994. Rapid atmospheric fronts arriving from the west covered the area during the two preceding days; the sea was then calm. In the partial image of 10 September; the distribution of the water masses was

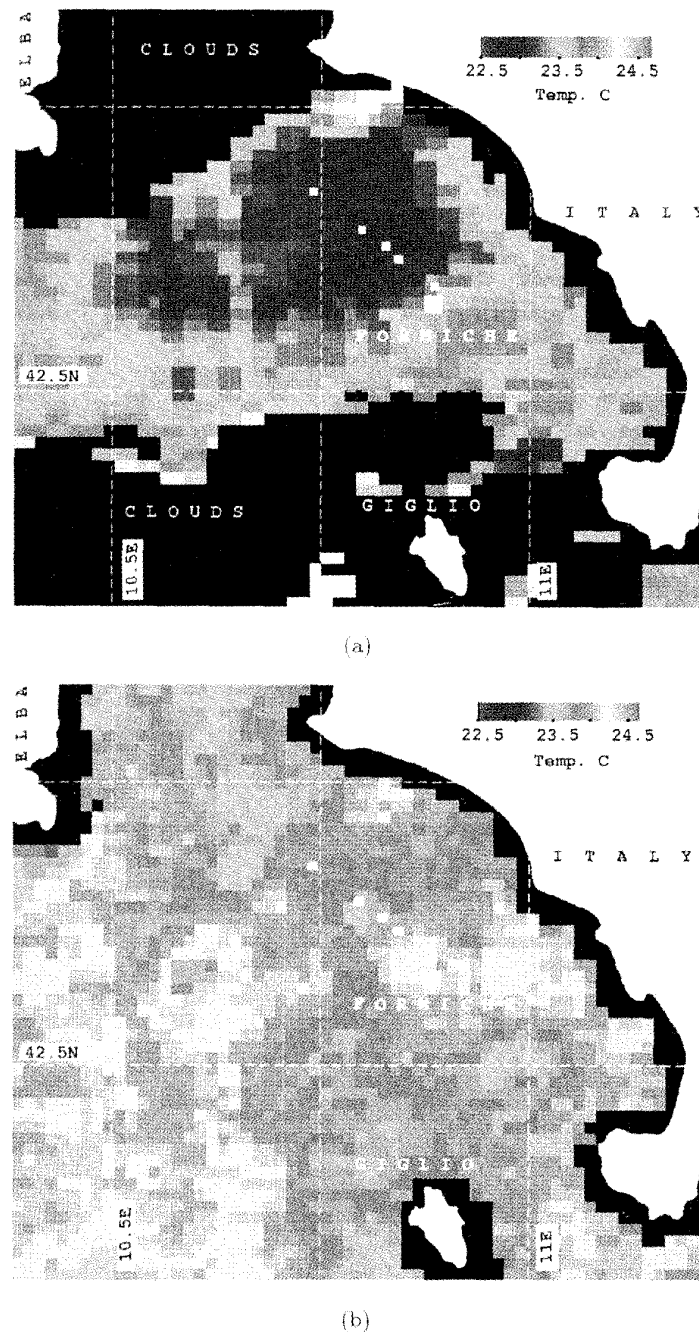


Fig. 4. Sea-surface temperature (SST) over the experimental area; (a) 10 September 1994 1628 UTC, (b) 11 September 1616 UTC. SST was calculated from channels 3 and 4 of the NOAA11 advanced very high resolution radiometer (AVHRR) using Bernstein's algorithm; the image was transformed in Mercator projection. Each cell represents an area of  $1.1 \text{ km} \times 1.1 \text{ km}$ . The white squares indicate the position of the acoustic moorings.

not yet bright [Fig. 4(a)]. The sea surface lost heat as a result of the cold winds. The lowest surface temperature along the transect was  $22.8 \text{ }^\circ\text{C}$  at 9-km range, and the highest,  $23.4 \text{ }^\circ\text{C}$  at 0 km. On 11 September the whole image was cloud-free with a clearer distribution of the underlying water masses [Fig. 4(b)]. The overall temperature was warmer than on the previous day, ranging from  $23.5 \text{ }^\circ\text{C}$  at 9 km to  $24.2 \text{ }^\circ\text{C}$  at 0 km. Comparison of both images showed that the spatial variability remained

stable during the two days. In particular, the cooler region situated in the middle of the transect persisted over the two days.

2) *2-D Subsurface Profiling*: Two-dimensional (2-D) sound-speed structures along the YS94 transect were determined by using a towed oscillating system [37] equipped with a CTD that measures conductivity (to obtain salinity), temperature and depth. Conventional hydrographic measurements including

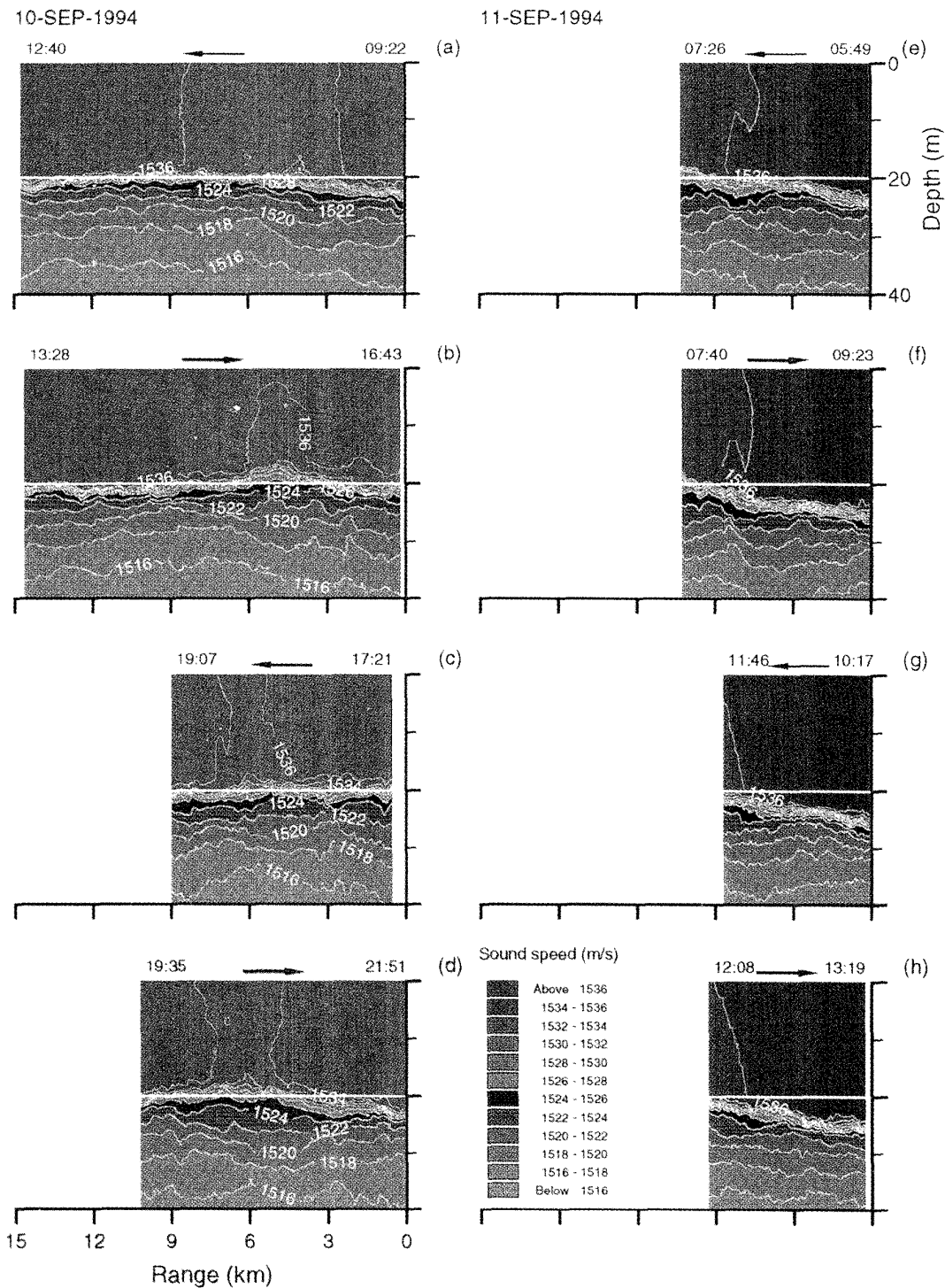


Fig. 5. Two-dimensional sound-speed structures along the YS94 transect obtained from towed oscillating CTD measurements during the acoustic runs. 10 September 1994: (a) 15-km LF, (b) 15-km HF, (c) 9-km LF, and (d) 9-km HF. 11 September: (e) 6-km LF, (f) 6-km HF, (g) 4.5-km HF, and (h) 4.5-km LF. The white line is a reference at 20-m depth. The range is referred to the receiving array at Formiche di Grosseto islands. The arrows show the direction of the survey.

CTD, XCTD, and XBT casts were performed for comparison and calibration purposes; conductivity and temperature at 4-m water depth were also measured by a keel-mounted sensor. The measurements were performed simultaneously

with the acoustic transmissions by R/V *Alliance* using DGPS navigation.

Fig. 5 shows the 2-D sound-speed structures observed along the YS94 transect during each acoustic run. The most variable

part of the water column is shown (upper 40 m). The structures were determined from CTD sections obtained with the ship sailing from the receiver to the source and back, during each acoustic run. This procedure and the satellite observation allowed to separate the spatial variability from the temporal. The sound speed exhibited temporal variability partly due to perturbed atmospheric conditions. The range-averaged thickness of the mixed layer increased over the two days. Comparison with Fig. 4 shows that the surface and subsurface temperature (sound-speed) structures were correlated. The feature at 6-km range remained stable during the two days. The range dependence was stronger on 11 September with a deepening of the mixed layer towards the receiving site. There was no significant range dependence in the salinity profiles. Table II gives statistics of the mixed-layer depth during the four acoustic runs.

Fig. 6 shows in more details the sound-speed variability during the 9-km range acoustic run. Comparison of pair of profiles taken from each section at a given range indicates that the lowering of the thermocline was a consistent time-dependent effect. At the array location the thermocline top depth increased by 6 m in a 4-h period. Closer examination of the two sections shows a region centered at 6-km range where the mixed layer is shallower than the overall temporal trend. This feature is correlated with the sea-surface temperature observations in Fig. 4(a) where a cooler region was located in the middle of the transect. The overall spatial/temporal variation in the thermocline part of the SSP had a profound impact on acoustic propagation especially at the upper frequencies and longer ranges (see Fig. 22).

Such detailed SSP data were exploited to invert the acoustic data and interpret the results.

#### D. Bottom Sediment Layers

The YS94 experimental area is part of the continental shelf facing southeastern Elba island and delineates the Giglio basin to the east (see Fig. 7). The passage basin-platform is not well defined but is certainly west of the YS94 transect.

Geophysical surveys were conducted in February 95 by R/V *Alliance* and in May 95 by R/V *Manning* to characterize the seafloor morphology and surficial sediments along the YS94 and YS95 transects. Seismic reflection data obtained along the YS94 transect and selected core data collected on the platform are interpreted.

1) *Acoustic Stratigraphy*: High-resolution, single-channel seismic reflection profiles were obtained along the YS94 transect. Short pulses of 1-ms duration and 300-J energy were transmitted every 0.7 s from an impulsive source (boomer) towed less than 20 cm below the sea surface at a speed of 2.3 m/s (see Fig. 8). Most of the boomer energy was in the 1–4-kHz frequency band. The transmitted pulses were recorded on a hydrophone towed at 13-m water depth and the bottom-reflected signals were recorded on a short 10-element array towed less than 10 cm below the sea surface. The seismic traces (one every 1.6 m) were digitized and processed with the DGPS navigation data to obtain an accurate profile of the sediment layers.

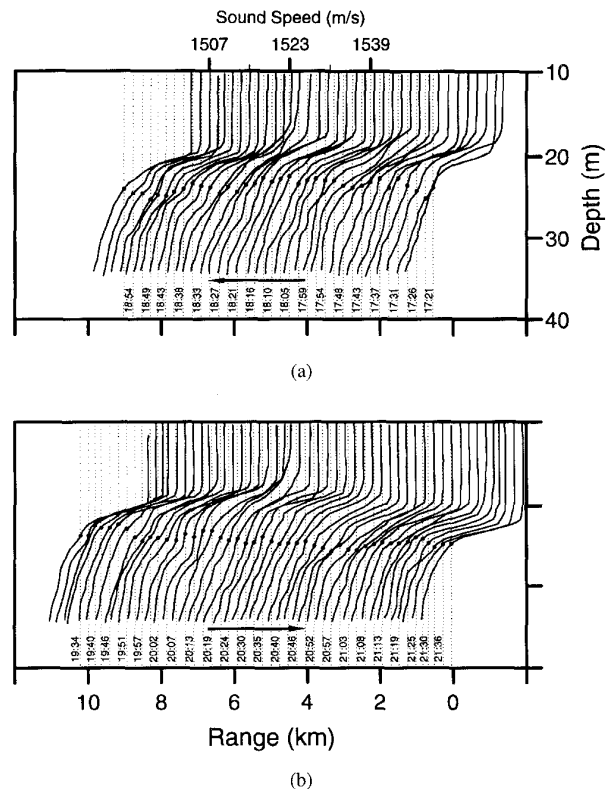


Fig. 6. Sound-speed profiles along the YS94 transect during the 9-km acoustic runs; (a) from receiver to source, (b) and back. The range is referred to the receiving array at Formiche di Grosseto islands. The arrows show the direction of the survey ship. The dot and vertical line on each profile indicate the mid value of the sound-speed scale, and point to the corresponding range and UTC time.

The raw signals were first deconvolved to remove the source transfer function, and then deghosted to remove the sea-surface reflection near the receiver. Deghosting consists of deconvolving the received signal with a receiver-ghosted model of the transmitted pulse. The source-ghost present in the recorded transmitted signal is already accounted for in the deconvolution. The signal-to-noise ratio (SNR) of the received signals was improved by ensemble averaging. Fig. 9 shows a sample of raw and processed seismic signals. The processing provided a sharper profile and the true echo character; comparison of Fig. 9(b) and (d) shows that the bottom-reflected signal is restored into a single peak.

Fig. 10 shows the seismic profile of the YS94 transect obtained from the processed seismic traces. The detailed bathymetry was obtained from the two-way travel (TWT) time calibrated with the depth-averaged sound speed measured during the seismic run (YS95). The bottom is fairly flat over the entire transect; the water depth varies by less than 4 m.

In the present highstand, a platform sediment is being deposited in a concordant way on littoral deposits from the last regression [39], [40]. The first layer made of pelite is homogeneous with thickness varying between 5 m and 9 m. The irregular bottom features in the 6–15-km segment are mostly due to subareal erosion during the last regression.

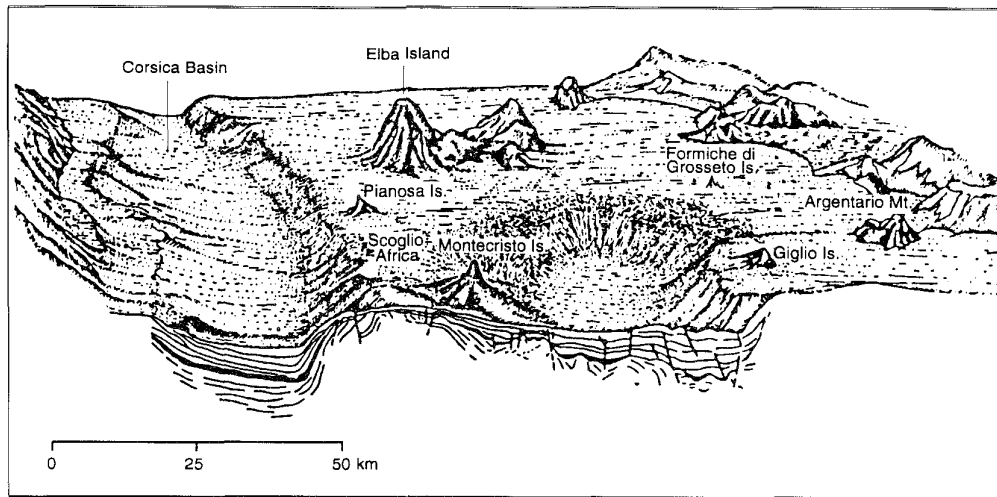


Fig. 7. Morphology of southern Toscana continental margin (after Wezel *et al.* [38]).

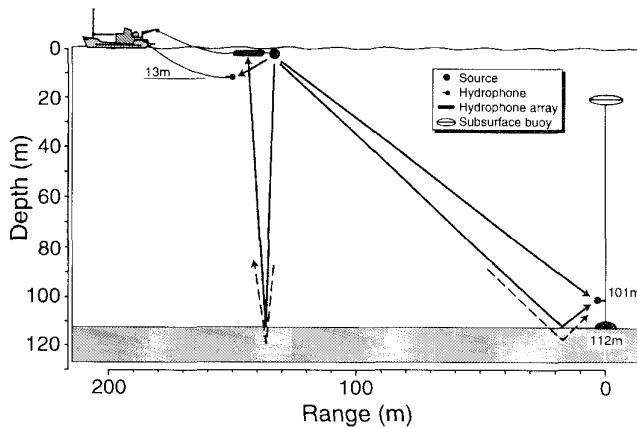


Fig. 8. Geometry for seismic reflection measurements along the YS94 transect on 5 May 1995.

The prolonged echoes of the second reflector reveal a thin and inhomogeneous layer of sand. The prominent third reflector in the 7–14-km segment indicates a depression that was filled with sediments during the last depositional sequence. On both sides of the depression these sediments were completely eroded so that older, and probably more consolidated sediments, are present.

The depth variations of the water-bottom and clay-silt interfaces correspond to less than 4% of the water depth. Table 2 gives statistics of the water depth and top layer thickness for the four measuring ranges.

2) *Inversion of Acoustic Reflectivity Versus Angle:* At the array location the direct and bottom reflected arrivals from the towed boomer were recorded on a hydrophone suspended 11 m above the bottom (Fig. 8). Fig. 11(a) shows the signals reflected at the interface of the first and second sediment layers as a function of range. The reflection coefficients as a function of incidence angle were measured for the two interfaces. The compressional wave speeds and densities of the two layers were then estimated (see e.g., [41]). The reflection coefficients were determined from the ratio of the square-rooted energies

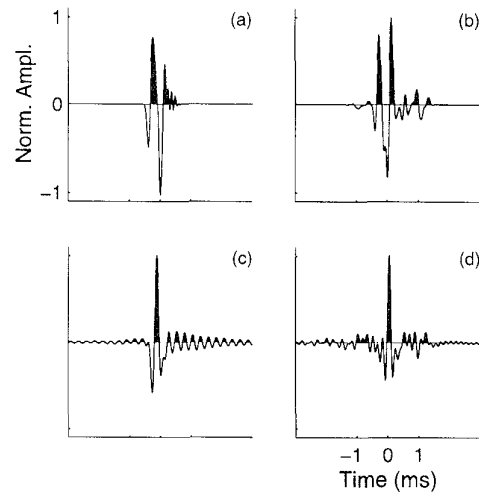


Fig. 9. Seismic processing. (a) Raw transmitted pulse. (b) Raw echo (first bottom reflection). (c) Deghosted transmitted pulse. (d) Deconvolved/deghosted echo.

in the direct and reflected arrivals after bandpass-filtering (1 kHz–2.8 kHz) to enhance the SNR [Fig. 11(b)]. Additional geometrical spreading in the reflected arrivals and TL through the first layer were corrected for.

For a fluid-fluid interface with sound speeds  $c_1$  and  $c_2$  and densities  $\rho_1$  and  $\rho_2$  the reflection coefficient as a function of incidence angle  $\theta_1$  is given by

$$R(\theta_1) = \frac{\rho_2 c_2 \cos \theta_1 - \rho_1 c_1 \cos \theta_2}{\rho_2 c_2 \cos \theta_1 + \rho_1 c_1 \cos \theta_2} \quad (1)$$

The Snell's law is

$$\sin \theta_1 / c_1 = \sin \theta_2 / c_2. \quad (2)$$

For known run geometry, and known sound speed and density above the interface a least-square fit to the reflection versus angle data yields the sound speed and density below the interface [Fig. 11(c) and (d)]. Because of the poor SNR of the reflected arrivals, the measured reflection coefficients, and

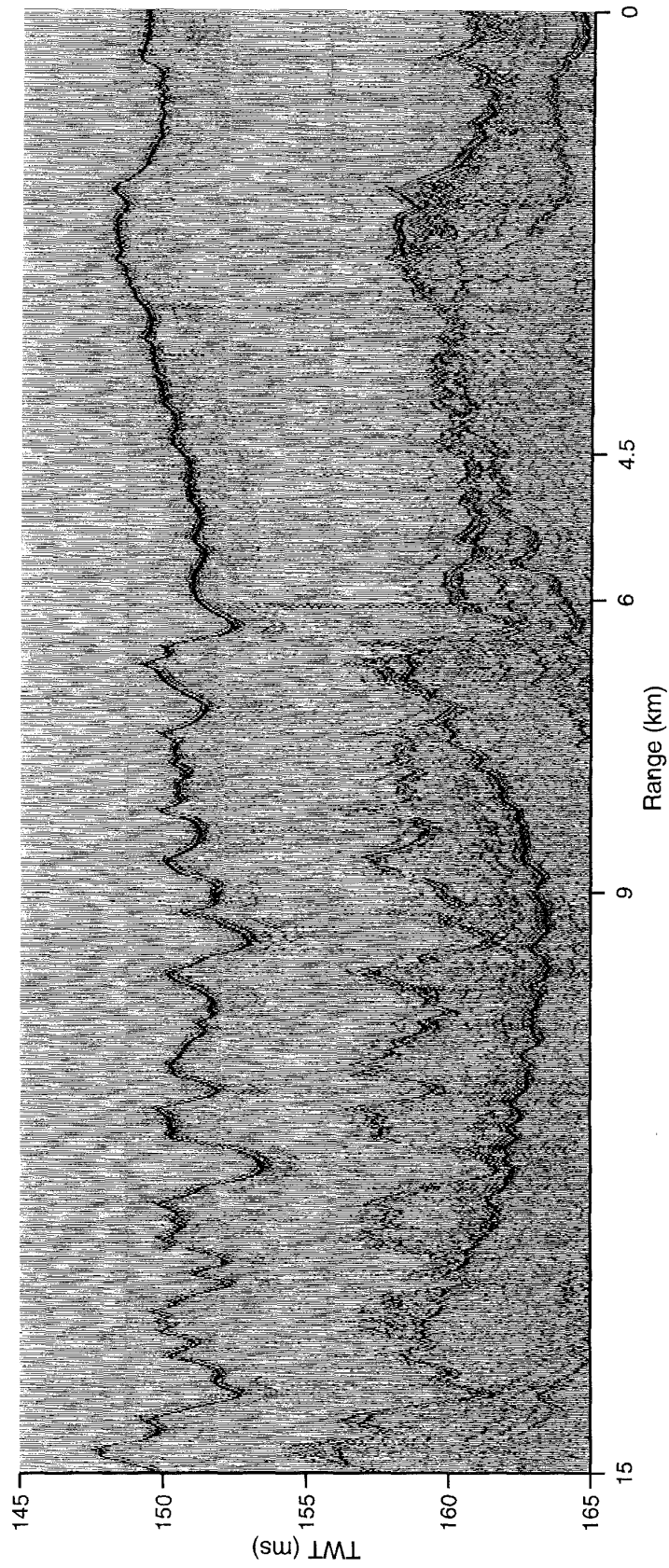


Fig. 10. Seismic reflection profile of the two upper sediment layers along the YS94 transect. For display purpose time-exponential weighting was applied to the traces. Positive peaks are shaded. The range tickmarks indicate the position of the deployed sound sources and the fixed receiving array (0 km). The depth-averaged water sound speed was 1508.1 m/s.

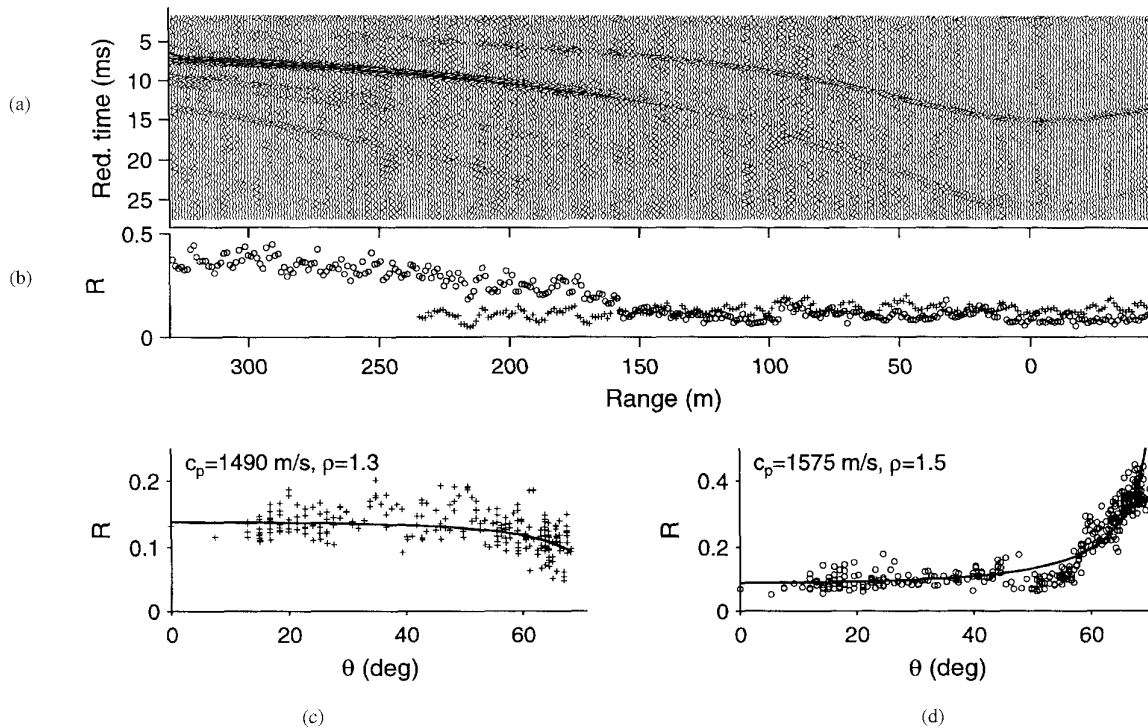


Fig. 11. Inversion of reflection vs angle data. (a) Signals reflected at the interface of the first and second sediment layers versus range (time is referred to the direct arrival). (b) Reflection coefficient vs range for the first (+) and second (o) interfaces. (c) Reflection coefficient versus incidence angle (+) and fitted curve (solid) for the first interface. (d) Reflection coefficient versus incidence angle (o) and fitted curve (solid) for the second interface.

the estimated sound speeds and densities, are expected to be slightly larger than the true values. Also the reflection at the second interface is affected by the thin sand layer. In spite of the limited spatial coverage these results provided an independent characterization of the sea bottom.

3) *Sediment Cores*: A set of 16 cores were collected with a gravity corer by R/V *Alliance* at characteristic locations in the basin. The core tubes had a length of 3 m and a diameter of 11 cm. The coring locations were determined from DGPS-based seismic reflection profiles obtained along the YS94 and YS95 transects (see Fig. 2).

The compressional wave-speed profile was determined from travel-time measurements between a pair of 200 kHz transducers placed every 5 cm along the core tube. A correlator was developed at SAACLANTCEN to improve the time precision [42]. Error of less than 1 m/s can be obtained when the measurement is taken at constant temperature. In order to validate the measurement, the sound speed of the water contained in the upper part of the core was measured using the same instrument. The bottom-water sound speed determined from a CTD cast at the coring location was compared with the sound speed of the core water corrected to *in situ* pressure and temperature. Ideally the two sound-speed values should be equal; for most of the analyzed cores the difference did not exceed 3 m/s. The depth-dependent mass properties of the sediments were measured from samples taken at different core levels (every 5 cm as for the sound speed) using standard laboratory procedures. The core data were compared with other core data collected in the same area [43] and data reported in the literature [44], [45].

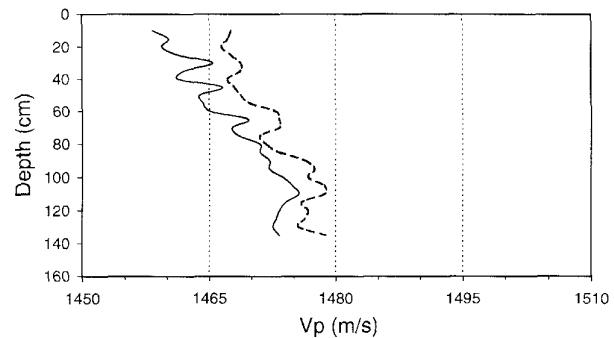


Fig. 12. Compressional speed in the upper part of the clay layer measured at the mid point of the YS94 transect (core 8, solid line), and at the vertical array location (core 9, dashed line). The bottom-water sound speed was 1509 m/s.

Fig. 12 shows the compressional speed measured from cores 8 and 9 along the YS94 transect. The depth-averaged sound speed (1470 m/s) is lower than any speed in the water column. Both cores are characterized by a platform sediment (offshore) made of pelite with a mean grain size that varies between 9 and 10  $\Phi$  [ $\Phi = -\log_2(\text{diameter})$ ]. At the midpoint of the YS94 transect (core 8), the sediment class changes with depth from clay (75% clay, 25% silt) to silty clay (68% clay, 32% silt). At the vertical array location (core 9), the sediment is classified as clay (72% clay, 27% silt). Accordingly the top speed (1465 m/s) is higher and the gradient ( $10 \text{ s}^{-1}$ ) is smaller than for core 8 (1460 m/s,  $15 \text{ s}^{-1}$ ). The speed gradient is expected to decrease with increasing depth. The depth-average sound

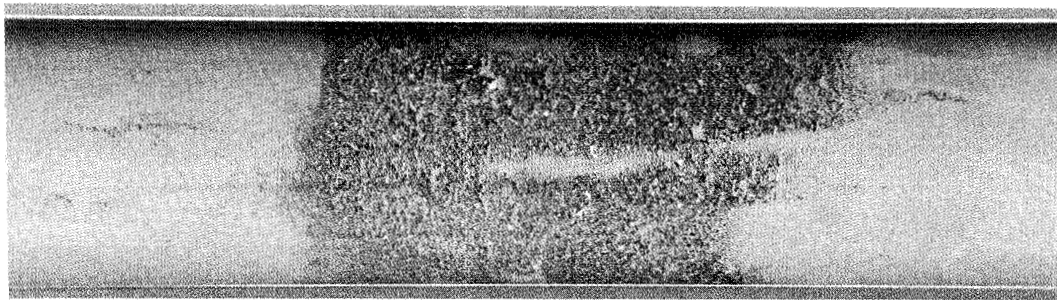
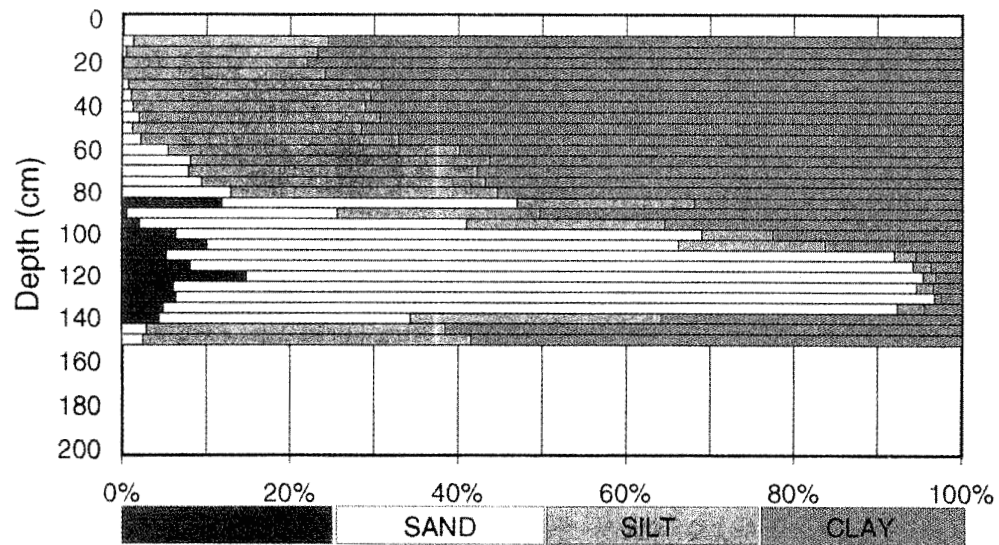
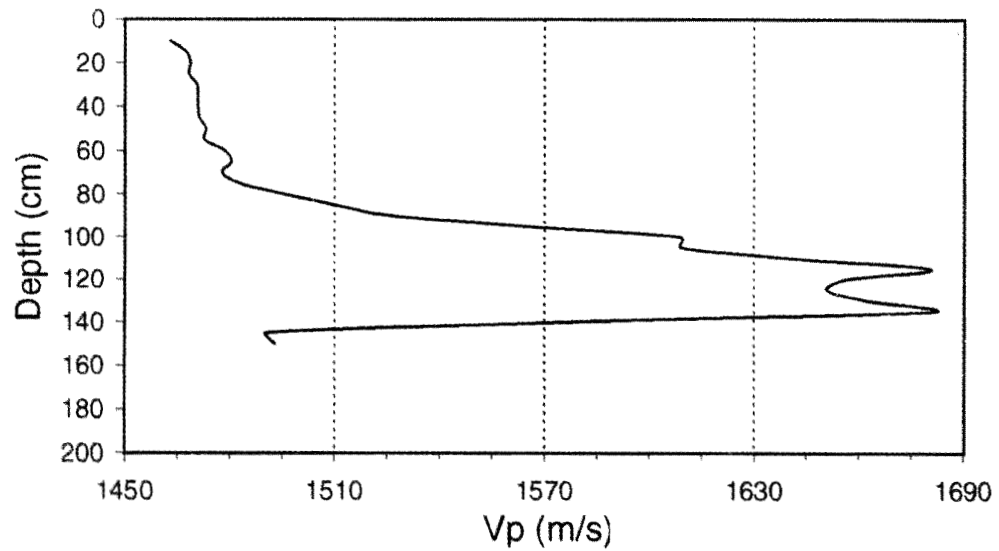


Fig. 13. Photograph of a characteristic core taken over an emerged sand dune near Elba island (core 2). The thickness of the sand layer is 30 cm. The second layer could be reached with a short corer only at such location. The top part of the core is on the left-hand side.



(a)



(b)

Fig. 14. Sand dune core data. (a) Gravel/sand/silt/clay distribution. (b) Compressional wave speed.

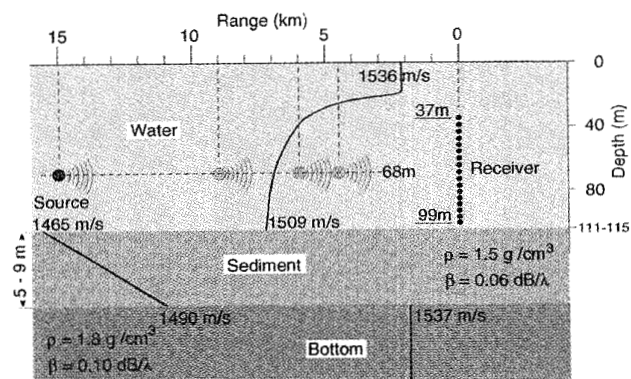


Fig. 15. Environmental model of the YS94 transect northwest of Formiche di Grosseto islands based on measured ocean sound-speed profiles and geoacoustic properties. The thin sand layer is not represented.

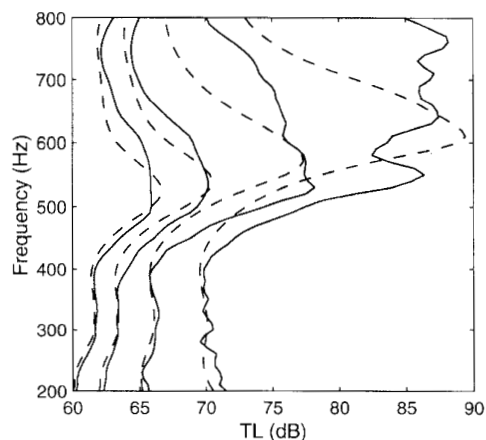


Fig. 16. Predicted frequency-dependent TL for the four measuring ranges based on the environmental model in Fig. 15 with range dependence of the bottom included (solid) and without (dashed); 4.5-km, 6-km, 9-km, and 15-km ranges from left to right. For the range-independent modeling, range-averaged values of water depth and top sediment thickness were taken for each range. The source and receiver (center of the array) depths are 68 m.

speed determined from the sediment cores agreed with the acoustic reflectivity inversion (Fig. 11). The measured wet density of  $1.5 \text{ g/cm}^3$  may be slightly larger than the true value due to the compaction of the sediment caused by the corer penetration. The reflectivity inversion yielded a density of  $1.3 \text{ g/cm}^3$ .

Deeper cores were not yet available at the time of writing. Full characterization required the extrapolation of data from other locations where the top layer could be fully sampled with the short corer. Only one of these cores is discussed here. Geological interpretation indicated that the deeper geoacoustic conditions along the YS94 transect can be inferred from core 2 collected near Elba island (see Fig. 2). This core was collected over an emerged sand dune where the first layer was particularly thin. The photograph in Fig. 13 shows the relict transgressive littoral deposits below the mud interval. The granulometric distribution and the compressional speed profile of core 2 are compared in Fig. 14. The core can be divided in three segments that represent the low-speed clay layer (above 80 cm), the sandy interface (85–140 cm) and the higher speed silt layer (below 145 cm). The acoustically-measured compressional

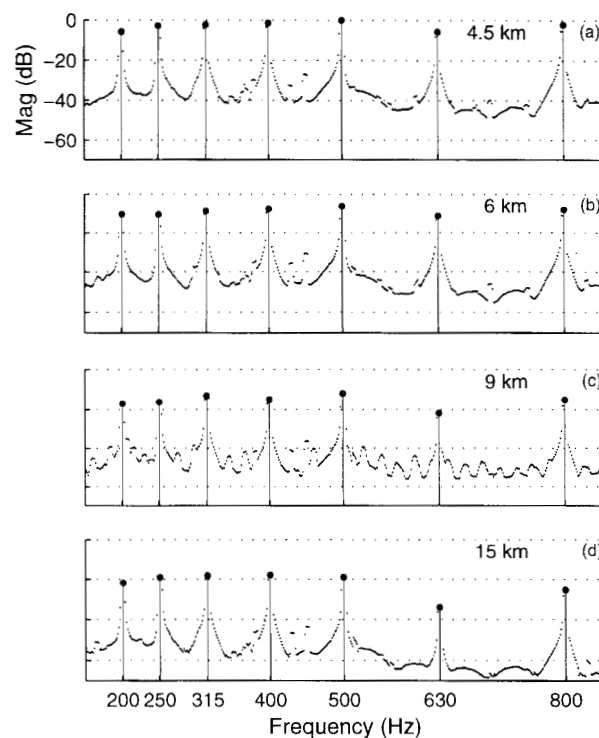


Fig. 17. Largest-eigenvalue "spectra" at each range: (a) 4.5 km, (b) 6 km, (c) 9 km, and (d) 15 km. The 0-dB level corresponds to the maximum power at the 4.5-km range. Transmitted power for the 15-km acoustic run was 3 dB lower than for the other runs.

sional speed profile was highly correlated with the mean grain size profile that resulted from the depth-dependent distribution of sand, silt and clay sediments. The first layer shows a positive gradient in compressional speed mostly due to the gradual increase of silt and sand content. At 75-cm depth the sound speed is 1490 m/s. The same behavior can be extrapolated to the much thicker top layer along the YS94 transect. At 80-cm depth sand begins to dominate and causes a marked increase of compressional speed (up to 1690 m/s). At 145-cm depth the sand content sharply decreases. Similar sand sediments are also present below the muddy shelf sediment northwest of Formiche di Grosseto islands. The vertical-incidence reflection data showed that the sand deposits are irregularly distributed in the horizontal (Fig. 10). Close examination of the seismic traces showed that there was no reflection from the clay-sand interface because of smooth impedance increase; a phase-reversed reflection occurs at the sand-silt interface as a result of the abrupt impedance decrease. At 145-cm depth the top part of the second layer has a higher compressional speed (1500 m/s) than the average speed of the first layer. The acoustic reflectivity inversion overestimated the sound speed of the silt layer due to the effect of the higher speed sand interface (Fig. 11).

#### E. YS94 Environmental Model

1) *Baseline Environmental Model:* Fig. 15 shows the environmental model derived from the measured oceanographic and geophysical data. The attenuation values were taken from [46].

TABLE III  
INVERSION MODEL A WITH PARAMETER SEARCH BOUNDS

Model parameter	Lower bound	Upper bound
<i>Geometric</i>		
source range (km)	$R-2$	$R+2$
source depth (m)	65	75
array depth (m)	96	104
array tilt (m)	-2	2
<i>Water</i>		
water depth (m)	110	118
<i>Sediment</i>		
sound speed, $c$ (m/s)	1460	1500
sound speed increase, $\Delta c(5 \text{ m})$ (m/s)	10	50
sound speed increase, $\Delta c(10 \text{ m})$ (m/s)	10	50
sound speed increase, $\Delta c(20 \text{ m})$ (m/s)	10	50
attenuation (dB/ $\lambda$ )	0.01	0.4

Each parameter was discretized into 128 values.  $R$  is the true measuring range (4.5 km, 6 km, 9 km, or 15 km). The array depth refers to the bottom hydrophone. The array tilt refers to the horizontal displacement of the top hydrophone (positive in the direction opposite to the source).

TABLE IV  
INVERSION MODEL B WITH PARAMETER SEARCH BOUNDS

Model parameter	Lower bound	Upper bound
<i>Geometric</i>		
array tilt (m)	-2	2
<i>Water</i>		
thermocline depth increase (m)	-2	2
water depth (m)	110	116
<i>Sediment</i>		
sound speed, $c$ (m/s)	1460	1500
sound speed increase, $\Delta c$ (m/s)	5	50
layer thickness (m)	1	20
attenuation (dB/ $\lambda$ )	0.01	0.4
<i>Bottom</i>		
sound speed, $c$ (m/s)	1520	1630

Each parameter was discretized into 128 values. The thermocline depth increase is handled as a vertical translation of the whole SSP.

In summary, the water column was characterized acoustically by a strongly downward refracting sound-speed profile. The depth of the mixed layer was slowly time-varying with moderate range dependence. The propagation below the well-developed thermocline was not affected by sea-surface scattering effects. The bottom is nearly flat and characterized by a low-speed clay layer of variable thickness overlying a higher speed silt layer with some intermixed sand at the interface; the subbottom is made of similar consolidated sediments. The compressional speed and gradient in the sediments are mildly range dependent.

Although this model cannot be fully qualified as "ground truth" it serves as a baseline for comparing the inversion results presented in Section IV.

2) *Effect of Bottom Variability*: The frequency-dependent propagation effects over a soft top layer were explained theoretically in [47] and verified experimentally for the YS95 Elba-Formiche transect in [29]. In the latter range dependence of the geoacoustic properties in the platform was evidenced from geological data interpretation and broad-band data/model comparisons. The propagation effects due to a 1-m thick sand layer were modeled and interpreted in [34]; for a 30-cm thickness no strong influence is expected in the 200–800-Hz frequency band. In Fig. 16, the effect of bottom variability

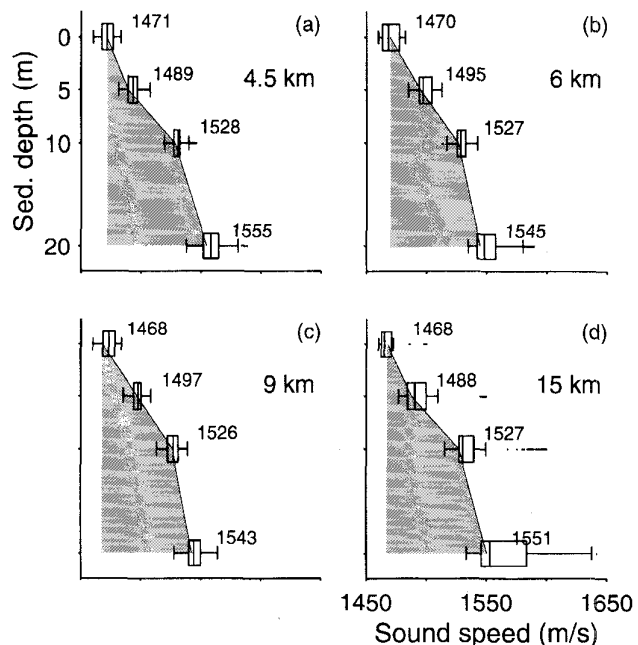


Fig. 18. Compressional-speed profile in the sediments obtained from broad-band inversion of one signal realization at each range: (a) 4.5 km, (b) 6 km, (c) 9 km, and (d) 15 km. The sound-speed scale corresponds to the search interval. The solid line shows the GA-mean of the *a posteriori* distribution weighted with fitness. The box plotted at each preset depth is a measure of the central tendency and dispersion of the unweighted *a posteriori* distribution. The left and right lines of each box are the 25th and 75th percentiles of the samples; the width is the interquartile range. The middle line is the median of the samples (50th percentile). Skewness is indicated by a non centered line. The lines extending to both sides of the box show the extend of the rest of the samples. Dots indicate outliers, i.e., values that are more than 1.5 times the interquartile range away from either side of the box.

on the broad-band propagation is shown by comparing range-independent (RI) and range-dependent (RD) predicted TL for the four measuring ranges. As the source is moved away from the receiving array the range-averaged thickness of the top soft layer decreases (see Fig. 10) and the frequency of the RI propagation null increases as explained in [29]. The RI- and RD-predicted TL differences increase with range and frequency. The frequencies above 400 Hz are affected by the bottom variability. In addition, sea-bottom and sea-surface scattering effects also affect the propagation at these frequencies.

### III. BROAD-BAND MATCHED-FIELD INVERSION

The broad-band inversion procedure presented herein is based on the matched field processing of acoustic-pressure observations across an  $N$ -element vertical array  $q(\omega)$ ,  $i = 1, 2, \dots, N$  at a number of frequencies. The inversion process includes an environmental model, a forward acoustic propagation model to predict the received pressure fields, a multi-frequency objective function to be optimized, and an efficient algorithm for searching the environmental parameter space. The environment is described by the model vector  $\mathbf{m}$ ,  $j = 1, 2, \dots, M$ . The objective function  $\Phi$  is a function of predicted (replica) field vectors  $\mathbf{w}(\mathbf{m}, \omega)$  and measured spatial correlation matrices  $\mathbf{R}(\omega)$  at the frequencies  $\omega_l$ ,  $l =$

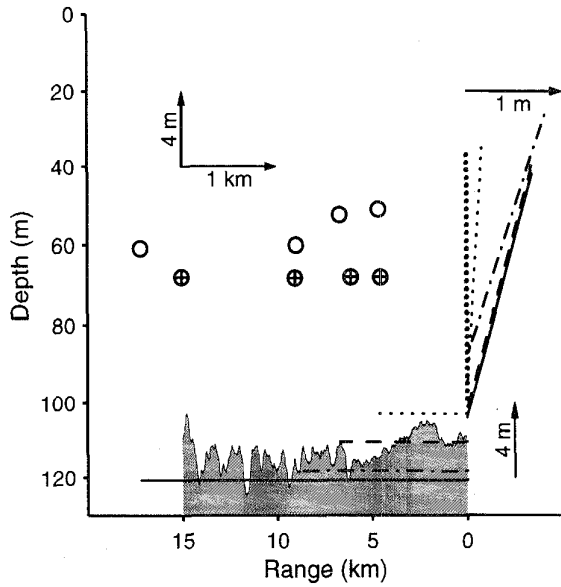


Fig. 19. Estimated geometric parameters for each measuring range: 4.5 km, 6 km, 9 km, and 15 km. True source ( $\oplus$ ) and receivers ( $\circ$ ) positions are indicated. The position errors are magnified about the true values in both range and depth as indicated by the arrows. The bathymetric variations (gray) are magnified about the range-averaged value.

1, 2,  $\dots$ ,  $L$ . The inverse problem is solved as an optimization problem, i.e., find the model vector  $\mathbf{m}$  that minimizes the objective function. Genetic algorithms (GA) were used for the optimization [32].

#### A. Maximum-Likelihood Objective Function

Under simplifying assumptions about signal and noise a generalized maximum likelihood estimate of the model vector  $\mathbf{m}$  is obtained by minimizing the function

$$\Phi(\mathbf{m}) = \frac{1}{L} \prod_{l=1}^L \left[ \text{tr} \hat{\mathbf{R}}(\omega_l) - \frac{\mathbf{w}^\dagger(\mathbf{m}, \omega_l) \hat{\mathbf{R}}(\omega_l) \mathbf{w}(\mathbf{m}, \omega_l)}{\mathbf{w}^\dagger \mathbf{w}} \right] \quad (3)$$

where  $\text{tr}$  is the trace operator and  $\dagger$  is the Hermitian transpose operator. The objective function in (3) is related to the linear (Bartlett) processor  $\mathbf{w}^\dagger \mathbf{R} \mathbf{w}$ . For a single frequency  $\omega$ , (3) reduces to

$$\Phi(\mathbf{m}) = \text{tr} \hat{\mathbf{R}}(\omega) - \frac{\mathbf{w}^\dagger(\mathbf{m}, \omega) \hat{\mathbf{R}}(\omega) \mathbf{w}(\mathbf{m}, \omega)}{\mathbf{w}^\dagger \mathbf{w}} \quad (4)$$

Equation (3) does not include the absolute or relative levels of the frequency-dependent transmission loss (TL).

#### B. Multitone Data Processing

Because of the high SNR, a good estimate of the correlation matrix at each frequency was obtained from a single 12-s realization of the signal. The observation interval was segmented into  $K = 17$  frames of duration  $T = 0.667$  s. Each time frame was Fourier transformed using the multiple-windows technique described in [48] and [49],

$$\mathbf{x}_{k,p}(\omega) = \mathcal{F}[\nu^{(p)}(T, W) \mathbf{x}(t + kT)] \quad (5)$$

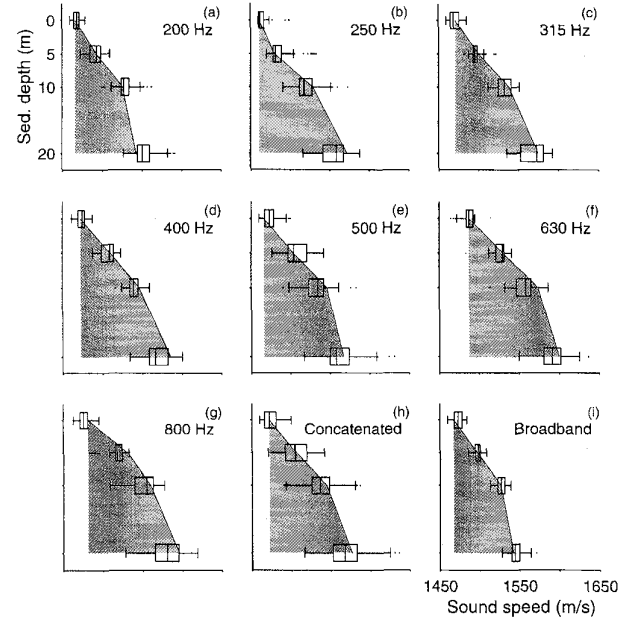


Fig. 20. GA-mean (solid) and descriptive statistics (box) of the compressional wave-speed profile estimated at each frequency for the 9-km range. (a)–(g) Single-frequency inversions. (h) Concatenation of all single-frequency inversions. (i) Broadband inversion. See Fig. 18 for an explanation of the box plots.

where  $\nu^{(p)}(T, W)$  is a set of  $P = 4$  orthonormal data tapers constructed as Slepian processes; the resulting bandwidth was  $W = 3.3$  Hz. The correlation matrix  $\hat{\mathbf{R}}$  was estimated at each tone frequency  $\omega_l$  as the ensemble average

$$\hat{\mathbf{R}}(\omega_l) = \frac{1}{KP} \sum_{k=1}^K \sum_{p=0}^{P-1} \mathbf{x}_{k,p}(\omega_l) \mathbf{x}_{k,p}^\dagger(\omega_l) \quad (6)$$

where  $KP = 68$ . Fig. 17 shows the largest eigenvalue from the eigen decomposition of the frequency-dependent correlation matrix for the four source ranges; which is an estimate of the signal plus noise received on the array. The sound pressure level at the source was equalized for the seven tones so that the observed differences in signal strength are only due to the frequency-dependent TL. The TL at 630 Hz is higher than at the other frequencies due to mode filtering effect in the soft surficial sediment as shown in Fig. 16.

#### C. Parameterization of the Environment

The design of a model that adequately describes the investigated environment is essential to obtain proper inversion results. This parameterization of the environment is a human-directed task based on waveguide physics and *a priori* information. Once a proper set of environmental parameters is chosen, the unknown parameters remain to be determined by optimizing the data/model match.

In the present case, experience was gained from related broad-band TL measurements [29] and the geoacoustic measurements discussed in Section II. The environmental model derived in Section II was taken as a baseline for the inversion process.

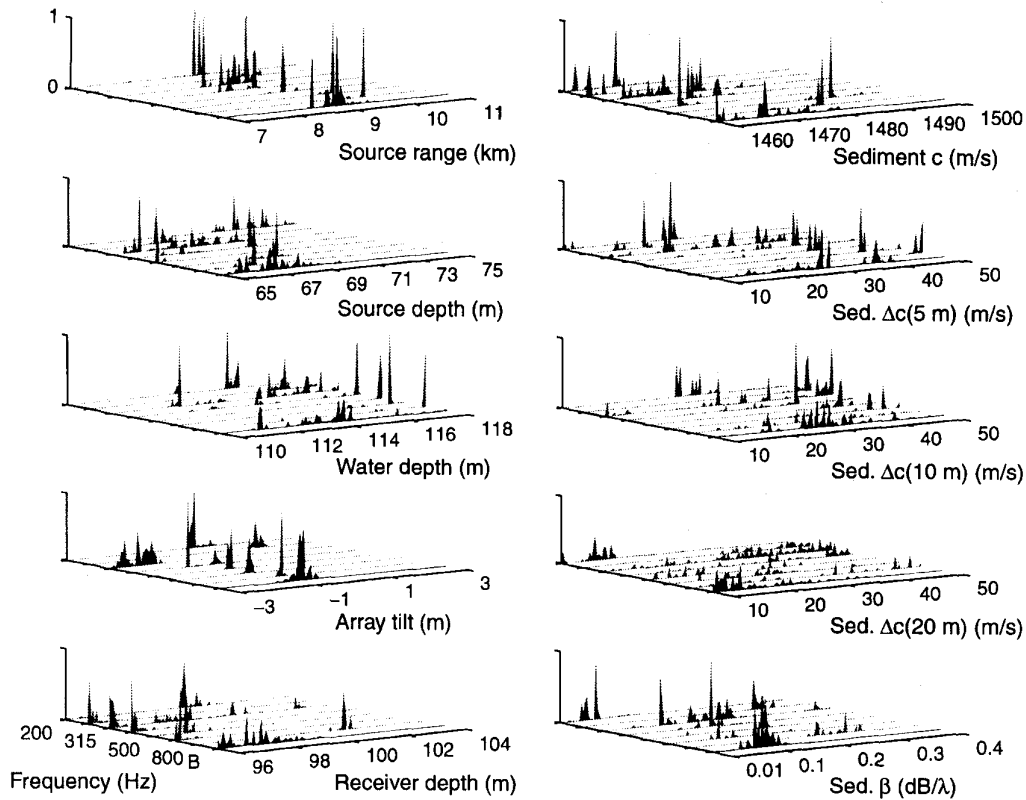


Fig. 21. *A posteriori* distributions for the single-frequency (gray) and broad-band (denoted B, black) inversions of Model A at 9-km range. The distributions are weighted with fitness.

Range-independent modeling was chosen to obtain integral properties of the mildly range-dependent YS94 transect. The acoustic fields were predicted with the normal-mode acoustic propagation model SNAP [50] where the environment is represented by three layers: a water layer, a fluid sediment layer and a homogeneous half-space layer.

To address the parameterization problem two environmental models were defined: an empirical model (A) and a data-oriented model (B).

In Model A, the available environmental information is virtually ignored (Table III). The geometric parameters of the experimental setup are treated as unknowns. A generic profile is used for the sound speed in the sediments and in the bottom (defined here as the half-space layer of the normal-mode propagation model).

In Model B, some *a priori* information about the specific environment was incorporated (Table IV). Thus all measured geometric parameters are known except the array tilt that was not directly measured. The array tilt was inferred from water-current time series (magnitude and direction) measured near the top and bottom of the array as mentioned in Section II. In order to model the low-speed thick sediment layer overlying a higher speed layer, the bottom was explicitly described by a two-layer model.

The selected search bounds for the parameters are given for both models in Tables III and IV. For those parameters that were not optimized the baseline values indicated in Fig. 15 were taken.

For inversion of both models the ocean SSP's used by the forward model were obtained from the ensemble average of all profiles measured along the transect during the acoustic transmissions. In the present experimental setup where both source and receiver were positioned below a well-developed thermocline, the depth of the resulting propagation channel and associated sound-speed gradient were important. For the inversion of Model A the time variations of the effective channel depth are controlled by varying the water depth and keeping the mixed-layer depth fixed. Alternatively for Model B, the range-averaged mixed-layer and water depths are both optimized. The top depth of the thermocline is controlled by translating the whole SSP in the vertical but maintaining the bottom-water sound-speed constant. This *ad hoc* approximation is efficient since it reduced the description of the SSP to a single parameter and was certainly sufficient considering the known but unmodeled SSP range dependence.

For Model A the sound speeds in the sediments were linked together by means of shape functions [51]. The shape functions were chosen empirically as

$$c(5 \text{ m}) = c(0 \text{ m}) + \Delta c(5 \text{ m}) \quad (7)$$

$$c(10 \text{ m}) = c(5 \text{ m}) + \Delta c(10 \text{ m}) \quad (8)$$

$$c(20 \text{ m}) = c(10 \text{ m}) + \Delta c(20 \text{ m}) \quad (9)$$

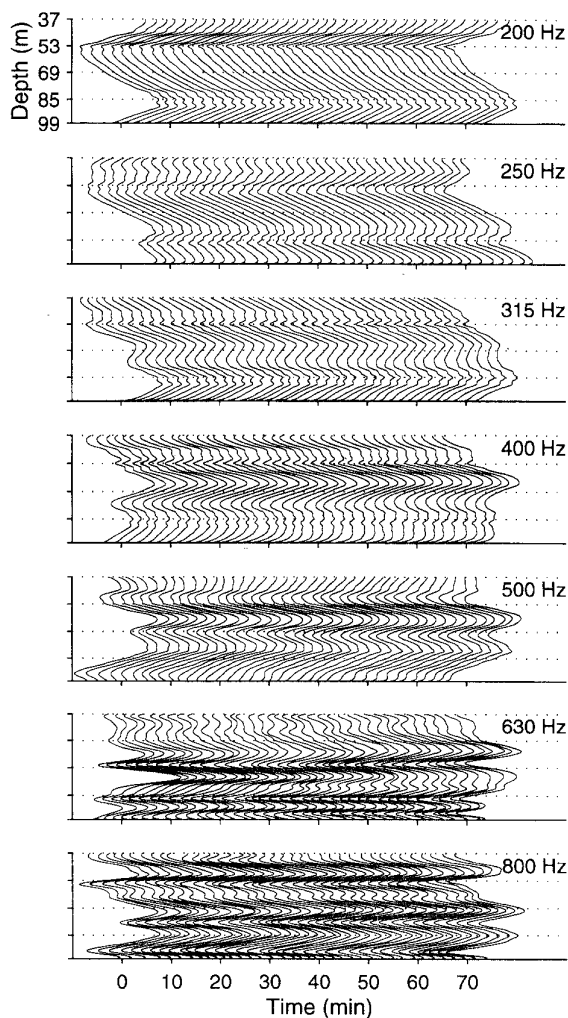


Fig. 22. Time variations of the pressure field received at 9-km range for a period of 74 min. The pulse repetition rate is 2 min. The magnitude of the first eigenvector from the eigenexpansion of the estimated correlation matrix is shown.

with constant gradient between these points. The bottom sound speed was taken as the constant  $c = c(20 \text{ m})$ . The GA optimization was performed over the three shape coefficients  $\Delta c$  between the bounds indicated in Table III. This representation of the sediments and bottom regularized the SSP such that positive gradients were forced.

#### D. GA Optimization and A Posteriori Analysis:

The SAGA [52] code was used for obtaining the set of model parameter values that yields the best match to the data. The GA search parameters were: population size of 64, reproduction size of 0.5, cross-over probability of 0.8, mutation probability of 0.05, number of iterations of 2000, and number of independent populations of 10.

A total of  $2 \times 10^4$  forward modeling runs were performed for each signal realization (number of iterations  $\times$  number of independent populations). For broad-band inversion the number of CW model runs increases linearly with the number of frequencies. After each inversion, 320 candidate solutions of the model vector  $\mathbf{m}$  were saved to analyze the convergence of

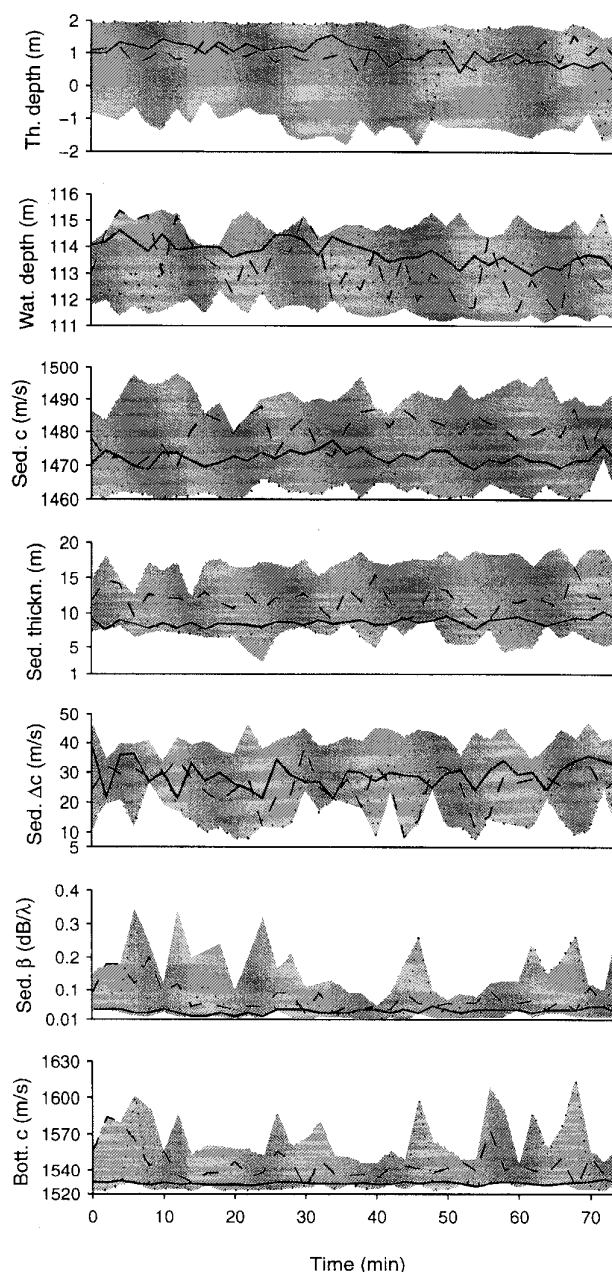


Fig. 23. GA-mean estimated values for Model B as a function of time: (solid) broad-band, (dot) 250 Hz, (dash) 500 Hz. The vertical scales correspond to the search intervals. The gray area represents the variation band of all single-frequency inversion results.

the algorithm (population size  $\times$  reproduction size  $\times$  number of independent populations).

In previous work, these solutions were weighted with their fitness before constructing the *a posteriori* distributions. Robust estimates were derived from the mean (GA-mean) of the resulting distribution. Weighting with fitness has the effect of focusing the distribution. In comparing the performances of the single-frequency and broad-band inversion techniques the *a posteriori* distributions were analyzed *prior* to weighting to determine their stabilizing effect. The final estimates were taken as the GA-mean of the weighted distribution.

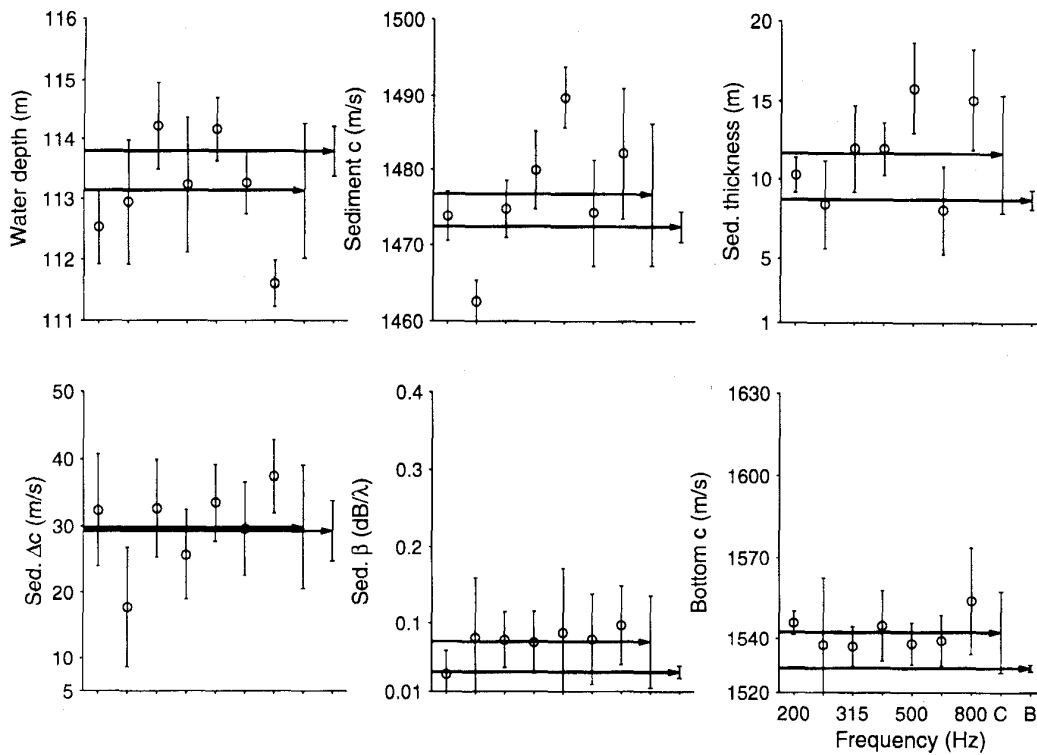


Fig. 24. Sample mean (circle) and one standard deviation (bar) of the GA-mean time series for the single-frequency, concatenated single-frequency (C), and broad-band (B) inversions of Model B. The vertical scales correspond to the search intervals.

#### IV. EXPERIMENTAL INVERSION RESULTS

Two data-processing scenarios were chosen to assess the performance of broad-band MFP inversion. The empirical Model A is inverted from one signal realization received at each range. The data-oriented Model B is inverted from all signal realizations received at 9-km range. For both scenarios the seven tones of the received pressure field were jointly processed in minimizing the objective function (3) (broad-band inversion) and separately processed using (4) (single-frequency inversion).

##### A. Empirical Model Inversion

1) *Integral Geoacoustic Properties:* Fig. 18 shows the compressional wave-speed profiles in the sediments determined from broad-band inversion at each range. The results were obtained from one signal realization at each range, i.e., a collection of seven correlation matrices estimated from a 12-s multitone signal. The estimated profiles are similar; the sound speeds at 0-m depth (in the slow sediment) and at 10-m depth (in the faster sediment) vary by less than 3 m/s across the four ranges. The upper gradient increase for the 6-km and 9-km measurements is consistent with the decreasing thickness of the soft top layer (see the reflection profile in Fig. 10) and the core data (compare the two sound-speed profiles in Fig. 12). The estimation at 20-m depth is more uncertain; as range, depth and frequency increase lesser bottom-interacted energy of the multitone signal contributes to the inversion process. The wavelength ranges from 1.9 m to 7.5 m and, as a rule of thumb, the penetration depth corresponds to a few

wavelengths. For the 15-km measurement the lower-gradient increase is probably due to integrated propagation effects over the depression where the top layer thickness decreases and the speed in the underlying layer increases (more consolidated sediments from an earlier depositional sequence). Unmodeled range dependence of the bottom and lower SNR explain the larger spread of the distribution. The estimated attenuation slightly increased with range; the obtained values 0.08–0.1 dB/ $\lambda$  are in agreement with other measurements based on frequency-dependent transmission loss [29]. It is stressed that the attenuation is determined from the shape of the complex pressure field across the array and not from transmission loss measurements. Broad-band inversion provided robust integral properties of the sediment considering that they were estimated from a single transmission at different distances under variable hydrographical conditions [Fig. 5(a), (c), (e), (h)]. This statement will be substantiated from other results presented below.

2) *Sanity Check with Geometries:* The known experimental geometries were inverted to validate the acoustic data. Fig. 19 shows the geometric parameters that were optimized together with the environment. The estimated ranges and depths of the source are close to the true values. The errors in source depth are such that the height from the bottom is preserved. The errors in source and receiver depth are in the same order as the water depth variation along the transect. The water depths are very close to the range-averaged values. The array tilt is consistent with the current magnitude and direction; the low SSE current nearly aligned with the transect slightly tilted the array in the direction opposite to the source.

3) *Broad-Band Versus Single-Frequency*: In Fig. 20, the results from single-frequency and broad-band inversions are compared. Comparison with the core and reflection data in Section II shows that the single-frequency inversions largely overestimated the sediment speed [solid line in Fig. 20(a)–(g)]. The associated distributions are widely spread and skewed (box plots). The broad-band inversion [Fig. 20(i)] yielded correct speed and gradient (see the core data in Fig. 12). The compactness of the distributions indicates the stabilizing effect of the multifrequency objective function in the convergence of the GA. There is no overall correlation between the single-frequency profiles and the broad-band profile. The 200-Hz profile is somewhat similar to the broad-band but the profile at the close frequency of 250 Hz differs significantly. The estimated gradients increase with frequency due to lack of sensitivity related to the effective penetration depth. In addition, the 630-Hz and 800-Hz profiles have a speed at 0-m depth much larger than the broad-band. The broad-band estimate of speed at 20-m depth is lower than any corresponding single-frequency estimate. To demonstrate that joint optimization across all frequencies is essential, the single-frequency distributions were concatenated for comparison with the broad-band [Fig. 20(h)]. Only in the broad-band case, the sample mean of the fitness-weighted distribution is very close to the median of the nonweighted distribution. In this case weighting with fitness does not improve the estimation. Comparison of the single-frequency and broad-band results for the three other ranges led to the same conclusions.

In Fig. 21, the *a posteriori* distributions resulting from the single-frequency and broad-band inversions are compared. The single-frequency distributions are frequency-dependent and dispersed, while the broad-band distributions are more compact and monomodal except for one parameter [ $\Delta c(5\text{ m})$ ]. This demonstrates the ability of the broad-band inversion in reducing ambiguities.

### B. Data-Oriented Model Inversion

Using Model B the relative performance of single-frequency and broad-band inversions is determined. In particular the stability of the bottom estimates with respect to ocean variability is investigated.

1) *Time-Varying Pressure Field*: Fig. 22 shows the time variations of the pressure field received at 9-km range for a period of 74 min. Because of the static configuration of the acoustic moorings the observed variability was attributed entirely to the ocean volume. The smooth variation of the received pressure field was due to time-varying thickness of the mixed layer and fluctuating sound-speed structure in the thermocline as described in Section II. All frequencies were affected with larger and shorter-term variations at the higher frequencies.

2) *Effect on Bottom Inversions*: The parameters of Model B were inverted separately for each of the 38 signals received over a period of 74 min. As for Model A the inversion was performed for each frequency individually and for all frequencies together. Fig. 23 shows the time histories of the GA-mean for the single-frequency and broad-band inversions.

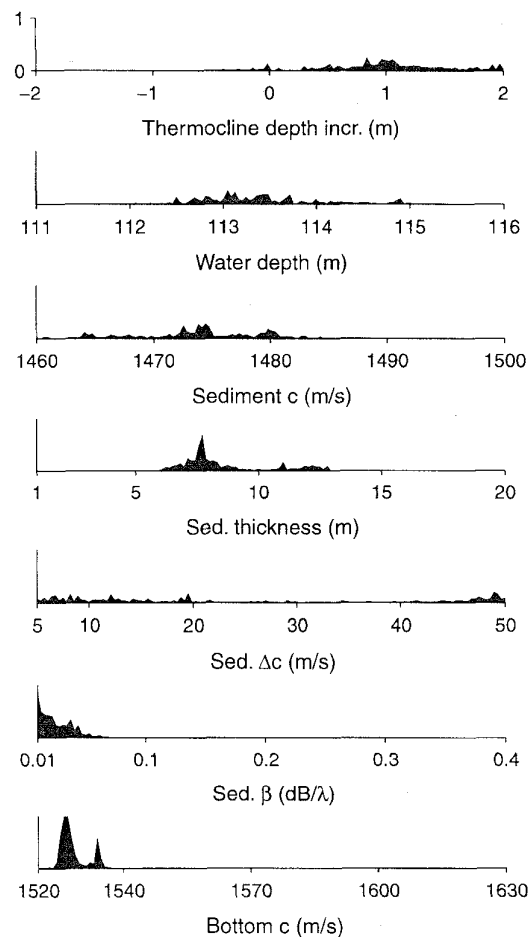


Fig. 25. Overall *a posteriori* distributions for the Model B. The results from the inversion of 38-signal realizations at 9-km range were concatenated into one single distribution. The distributions are weighted with fitness.

For each inversion run the GA-means were computed from the 320 candidate solutions. The fluctuations in ocean sound speed [Fig. 6(a)] cause large variations of the single-frequency bottom estimates (only shown for 250 Hz and 500 Hz). The variations seem random with no obvious relationship to the variations of the multitone pressure field shown in Fig. 22. The effect of ocean variability on each parameter is strongly frequency-dependent. The envelope of the gray area represents the overall variability across the seven individual frequencies. In comparison, the broad-band inversion (solid line) provides remarkable stability (Fig. 23).

3) *Broad-Band Versus Single-Frequency Statistics*: The statistics of the GA-mean time series for the single-frequency and broad-band inversions are compared in Fig. 24. For all parameters the bias and variance of the broad-band estimates are much smaller than the ones at the individual frequencies. As with Model A concatenating single-frequency results does not improve the estimation.

For the broad-band inversion, the candidate solutions obtained from the 38 signal realizations were concatenated into one collection of samples. Fig. 25 shows the resulting *a posteriori* probability distributions for all Model B parameters except the array tilt. The latter, the only geometric parameter

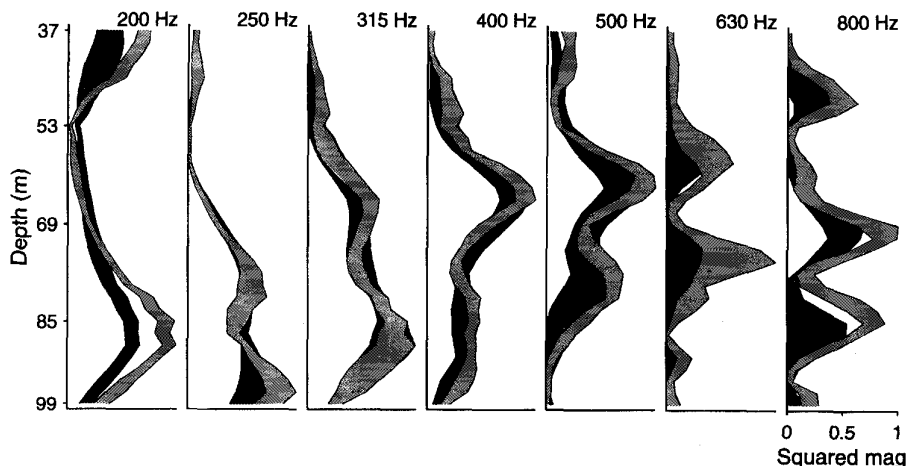


Fig. 26. The best global matches obtained from the 9-km data set using Model B. The light gray area represents the normalized squared-magnitude of the measured field and its variability over a 74-min period. The dark gray area is the corresponding Bartlett power obtained with the modeled fields.

that was inverted for in Model B, was very stable (0.5 m) and consistent with the water-current data as for Model A.

Clearly, the results shown in Figs. 23 and 25 are related. Based on the same data set the solid line in Fig. 23 emphasizes the variability of the broad-band estimates as a function of time, whereas Fig. 25 emphasizes the resulting spread over the search interval.

The characterization of the sediments is in close agreement with both the baseline model and the inversion results obtained with the empirical Model A from one single transmission. In particular the depth-average sound speed and range-average thickness of the soft layer are well determined, but at the detriment of the gradient and attenuation estimation.

Fig. 26 shows the squared-magnitude of the pressure field measured across the array and the largest Bartlett powers obtained from the 38 signal realizations. The Bartlett power can be interpreted as the degree of phase matching weighted by the magnitude of the pressure field. Under noise-free conditions and with proper normalization a perfect match occurs when the two quantities are equal at each depth. Alternatively the complex-valued measured and predicted fields can be compared but the interpretation is less immediate. The match is quite good below 500 Hz. Above 500 Hz, the performance degradation is likely due to the unmodeled range dependence in the sea bottom and to the spatial variability of the ocean SSP. This is consistent with the predicted effect on the frequency-dependent TL in Fig. 16.

4) *Effect of RD Ocean SSP on Bottom Resolution:* For the 4.5-km transect, the variability in the bottom is small (Fig. 10) and does not strongly affect the broad-band propagation. This is verified by comparing the predicted TL versus frequency for RI and RD bottom models constructed from geophysical data (Fig. 16).

For that range, the measured 2-D ocean sound-speed structure was incorporated into the forward modeling. Fig. 27 shows the *a posteriori* distribution obtained from one signal realization with RD ocean SSP's. All geoacoustic parameters are correctly determined. In particular, when compared to RI

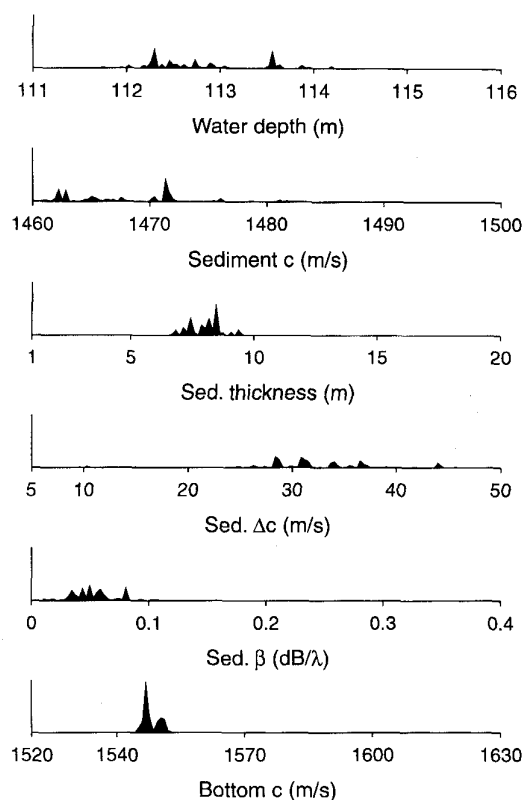


Fig. 27. *A posteriori* distributions obtained at 4.5-km range using Model B with range-dependent ocean SSP. The distributions are weighted with fitness.

case (not shown), the depth gradient of the sound-speed profile and attenuation are more accurate.

Fig. 28 shows the best global matches of the multitone pressure field obtained with RI and RD models of the ocean SSP. The RD ocean SSP information enhances the match for the upper-frequency components resulting in more accurate bottom inverses. The corresponding fit across all frequencies, as measured by the objective function (3), is significantly better

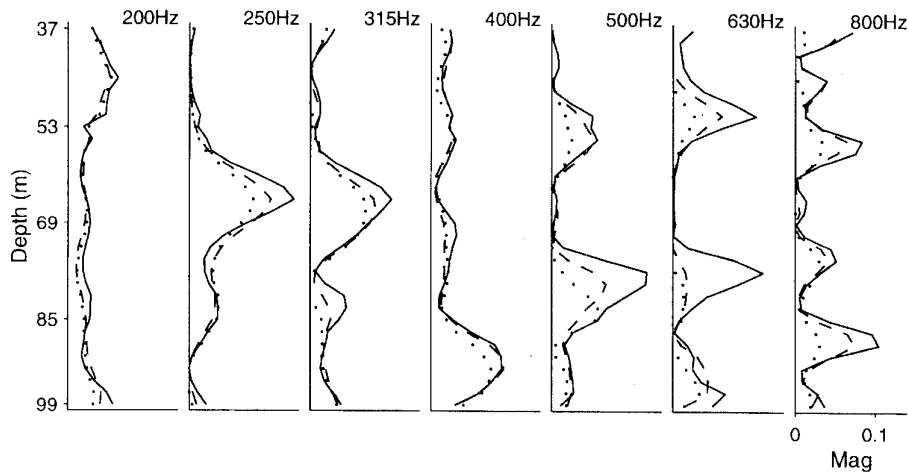


Fig. 28. The best match obtained from one signal realization at 4.5-km range using Model B with and without including the range dependence of the ocean SSP in the forward modeling. The RI (dotted) and RD (dashed) Bartlett powers are compared with the magnitude of the measured field (solid).

for the RD ocean SSP model ( $\Phi = 0.17$ ) than for the RI model ( $\Phi = 0.27$ ). This example showed that detailed bottom properties can be obtained if the bottom is reasonably RI and the RD of the ocean sound-speed profile is accounted for in the inversion.

#### V. CONCLUSION

Integral geoacoustic properties of the sea bottom were determined from inversion of broad-band, waterborne, acoustic propagation data. The data were collected during the YELLOW SHARK 94 experiment along a 15-km mildly range-dependent transect of 113-m water depth at a shallow water site, south of Elba island. Seven tones from 200 Hz to 800 Hz were transmitted simultaneously by a mid-depth acoustic projector bottom-moored at different ranges from a vertical array that spanned the water column below the thermocline.

The experimental geometries were fixed and accurately measured. Extensive environmental information was obtained *in situ* to support and validate the inversion. The 2-D ocean sound-speed structure across the tomographic sections was measured simultaneously with the acoustic transmissions. The sea bottom along the transect was independently characterized from geological interpretation, acoustic stratigraphy data, mass properties and compressional sound-speed measurements on sediment cores, and inversion of angle-dependent bottom reflection data.

Broad-band, matched-field inversion was implemented as follows. Matched-field processing was applied to the received pressure fields for each tone frequency. Optimization of the environmental parameters was performed simultaneously across all propagated frequencies. A maximum-likelihood objective function was derived which includes the linear (Bartlett) cross correlator at the individual frequencies. Genetic algorithms were applied to search for the global minimum of the objective function. The convergence and accuracy of the inversion were determined from statistical analysis of a *posteriori* distribution

of the candidate environmental models produced by the search algorithm.

Two range-independent bottom models were defined for the inversion: an empirical model with a generic sound-speed profile and a data-oriented model with a two-layer description derived from geophysical measurements.

For the experimental situation investigated, i.e., a fixed source-vertical array configuration and a few propagated modes, broad-band measurement was a *sine qua non* to obtain meaningful inversion results. By comparing inversion results at four different ranges, it was shown that representative, integral geoacoustic properties of the sea bottom were effectively determined within the constraints imposed by the bottom parameterization. The empirical model was more robust with respect to bottom variability in depth and range. By repeating the inversion every 2 min over 1 h it was demonstrated that broad-band inversion provided considerable stability with respect to ocean volume variability in time and space. Corresponding single-frequency inversions performed under the exact same conditions produced erratic results. By including range-dependent, ocean sound-speed profiles in the forward modeling, more detailed and accurate bottom inverses were obtained with the data-oriented model, in particular for the sound-speed gradient and attenuation of the low-speed top layer. The broad-band estimates of sound-speed profile, attenuation, density, and thickness of the top clay layer, and sound speed of the underlying silt layer, were in close agreement with the independent geophysical measurements. In conclusion, the broad-band inversion provided robust, unique and probably correct, integral geoacoustic properties of the sea bottom.

The YS94 acoustic propagation conditions were determined by a downward refracting ocean profile that maximized bottom interaction. During the YS95 experimental phase, acoustic data were obtained along the same transect with an identical tomographic configuration but with an isospeed ocean profile. The next step will be to compare the inversion results.

## ACKNOWLEDGMENT

The many people within and outside SACLANTCEN, and the crews of the R/V *Alliance* and *Manning* who participated in the YELLOW SHARK sea trials are warmly acknowledged for their outstanding contributions.

## REFERENCES

- [1] J.-P. Hermand, "The YELLOW SHARK broad-band inversion experiments," *IEEE J. Oceanic Eng.* (special issue on shallow water acoustics, geophysics and oceanography), July 1997, to be published.
- [2] W. Munk, P. Worcester, and C. Wunsch, *Ocean Acoustic Tomography*. New York: Cambridge, 1995.
- [3] A. Tolstoy, *Matched-field Processing for Ocean Acoustics*. Singapore: World Scientific, 1993.
- [4] H. P. Buckler, "Use of calculated sound fields and matched-field detection to locate sound in shallow water," *J. Acoust. Soc. Amer.*, vol. 59, no. 2, pp. 368–373, 1976.
- [5] A. Parvulescu, "Signal detection in a multipath medium by M.E.S.S. processing," *J. Acoust. Soc. Amer.*, vol. 33, p. 1674, 1961.
- [6] C. S. Clay, "Optimum time domain signal transmission and source localization in a waveguide," *J. Acoust. Soc. Amer.*, vol. 81, no. 3, pp. 660–664, 1987.
- [7] S. Li and C. S. Clay, "Optimum time domain signal transmission and source localization in a waveguide: Experiments in an ideal wedge waveguide," *J. Acoust. Soc. Amer.*, vol. 82, no. 4, pp. 1409–1417, 1987.
- [8] A. B. Baggeroer, W. A. Kuperman, and H. Schmidt, "Matched-field processing: Source localization in correlated noise as an optimum parameter estimation problem," *J. Acoust. Soc. Amer.*, vol. 83, no. 2, pp. 571–587, 1988.
- [9] E. K. Westwood, "Broad-band matched-field source localization," *J. Acoust. Soc. Amer.*, vol. 91, no. 5, pp. 2777–2789, 1992.
- [10] J.-P. Hermand and W. I. Roderick, "Model-based processing of large time-bandwidth product signals in a time dispersive ducted sound channel," in *Proc. NATO Advanced Study Inst. on Acoustic Signal Processing for Ocean Exploration*, J.M.F. Moura and I. M. G. Lourtie, Eds. Dordrecht: Kluwer, 1992, pp. 131–138.
- [11] ———, "Acoustic model-based matched filter processing for fading time-dispersive ocean channels: Theory and experiment," *IEEE J. Oceanic Eng.*, vol. 18, pp. 447–465, 1993.
- [12] ———, "Application of model-based matched filter processing to underwater acoustic inverse problems," in *Proc. Second Eur. Conf. Underwater Acoustics*, L. Bjørnø, Ed. Luxembourg: European Commission, 1994, pp. 381–386.
- [13] P. C. Mignerey and S. Finette, "Multichannel deconvolution of an acoustic transient in an ocean waveguide," *J. Acoust. Soc. Amer.*, vol. 92, no. 1, pp. 351–364, 1992.
- [14] I. T. Lu, H. Y. Chen, and P. Voltz, "A matched-mode processing technique for localizing a transient source in the time domain," *J. Acoust. Soc. Amer.*, vol. 93, no. 3, pp. 1365–1373, 1993.
- [15] S. M. Jesus, "Broad-band matched-field processing of transient signals in shallow water," *J. Acoust. Soc. Amer.*, vol. 93, no. 4, pp. 1841–1850, 1993.
- [16] R. K. Brienzo and W. S. Hodgkiss, "Broad-band matched-field processing," *J. Acoust. Soc. Amer.*, vol. 94, no. 5, pp. 2821–2831, 1993.
- [17] T. C. Yang, "Broad-band source localization and signature estimation," *J. Acoust. Soc. Amer.*, vol. 93, no. 4, pp. 1797–1806, 1993.
- [18] H. Y. Chen and I. T. Lu, "Localization of a broad-band source using a matched-mode procedure in the time-frequency domain," *IEEE J. Oceanic Eng.*, vol. 19, no. 2, pp. 166–174, 1994.
- [19] O. Diachok, A. Caiti, P. Gerstoft and H. Schmidt, Eds. *Full Field Inversion Methods in Ocean and Seismo-Acoustics*. Dordrecht: Kluwer, 1995.
- [20] C. L. Pekeris, "Theory of propagation of explosive sound in the ocean," *Geo. Soc. Amer. Mem.*, vol. 27, pp. 43–64, 1948.
- [21] W. A. Kuperman and F. B. Jensen, Eds. *Bottom-Interacting Ocean Acoustics*. New York: Plenum, 1980.
- [22] L. A. Rubano, "Acoustic propagation in shallow water over a low-velocity bottom," *J. Acoust. Soc. Amer.*, vol. 67, no. 5, pp. 1608–1613, 1980.
- [23] M. G. Brown, "Linearized travel time, intensity, and waveform inversions in the ocean sound channel—A comparison," *J. Acoust. Soc. Amer.*, vol. 75, no. 5, pp. 1451–1461, 1984.
- [24] J. Zhou, "Normal mode measurements and remote sensing of seabottom sound velocity and attenuation in shallow water," *J. Acoust. Soc. Amer.*, vol. 78, no. 3, pp. 1003–1009, 1985.
- [25] J. Zhou, X. Zhang, P. H. Rogers, and J. Jarzynski, "Geoacoustic parameters in a stratified sea bottom from shallow water acoustic propagation," *J. Acoust. Soc. Amer.*, vol. 82, no. 6, pp. 2068–2074, 1987.
- [26] S. D. Rajan, J. F. Lynch, and G. V. Frisk, "Perturbative inversion methods for obtaining bottom geoacoustic parameters in shallow water," *J. Acoust. Soc. Amer.*, vol. 82, no. 3, pp. 998–1017, 1987.
- [27] J. F. Lynch, S. D. Rajan, and G. V. Frisk, "A comparison of broad-band and narrowband modal inversions for bottom geoacoustic properties at a site near Corpus Christi, Texas," *J. Acoust. Soc. Amer.*, vol. 89, no. 2, pp. 648–665, 1991.
- [28] M. Badiey, I. Jaya, and A. H.-D. Cheng, "Shallow-water acoustic/geoacoustic experiments at the New Jersey Atlantic Generating Station site," *J. Acoust. Soc. Amer.*, vol. 96, no. 6, pp. 3593–3604, 1994.
- [29] J.-P. Hermand and R. Soukup, "Broad-band inversion experiment Yellow Shark '95: Modeling the transfer function of a shallow-water environment with a range-dependent soft clay bottom," in *Proc. Third Eur. Conf. Underwater Acoustics*, J. S. Papadakis, Ed., Heraklion, Crete, 1996.
- [30] S. Kirkpatrick, C. D. Gelatt, and M. P. Vecchi, "Optimization by simulated annealing," *Science*, vol. 220, pp. 671–680, 1983.
- [31] J. R. Koza, *Genetic Programming: On the Programming of Computers by Means of Natural Selection*. Cambridge, MA: MIT, 1992.
- [32] P. Gerstoft, "Inversion of seismoacoustic data using genetic algorithms and a posteriori probability distributions," *J. Acoust. Soc. Amer.*, vol. 95, no. 2, pp. 770–782, 1994.
- [33] P. Gerstoft and D. F. Gingras, "Parameter estimation using multifrequency range-dependent acoustic data in shallow water," *J. Acoust. Soc. Amer.*, vol. 99, no. 5, pp. 2839–2850, 1996.
- [34] J.-P. Hermand, "Model-based matched filter processing: A broad-band approach to shallow-water inversion," in *Full Field Inversion Methods in Ocean and Seismo-Acoustics*, O. Diachok, A. Caiti, P. Gerstoft, and H. Schmidt, Eds. Dordrecht: Kluwer, 1995, pp. 189–194.
- [35] J.-P. Hermand, F. Spina, P. Nardini, and E. Baglioni, "Yellow Shark broad-band inversion experiment: Environmental data 1994–1995," SACLANT Undersea Res. Centre, La Spezia, Italy, 1995, SACLANTCEN CD-ROM Yellow Shark series YS-1.
- [36] H.-H. Essen, E. Nacini, and P.-M. Poulain, "Comparison of satellite-retrieved sea-surface temperatures with drifter- and ship-borne measurements," SACLANT Undersea Res. Centre, La Spezia, Italy, 1996, SACLANTCEN document SM-297.
- [37] F. De Strobil and L. Gualdesi, "High resolution towed oscillating system," *Sea Technol.*, pp. 37–40, July 1994.
- [38] F. C. Wezel, D. Savelli, M. Bellagamba, M. Tramontana, and R. Bartole, "Plio-quaternary depositional style of sedimentary basins along insular tyrrhenian margins," in *Sedimentary Basins of Mediterranean Margins*, F. C. Wezel, Ed. Bologna, Italy: CNR Italian Project of Oceanography, 1981, pp. 239–270.
- [39] E. Michelozzi, "Quaternary sediments in the Elba-Formiche islands basin," SACLANT Undersea Res. Centre, La Spezia, Italy, 1994, SACLANTCEN document IN-678.
- [40] F. L. Chiocci, L. Orlando, and P. Tortora, "Small-scale seismic stratigraphy and paleogeographical evolution of the continental shelf facing the SE Elba Island (Northern Tyrrhenian Sea, Italy)," *J. Sedimentary Petrol.*, vol. 61, no. 4, pp. 506–526, 1991.
- [41] N. R. Chapman, K. Stinson, S. Levy, J. Cabrera, and D. W. Oldenburg, "Estimation of the elastic properties of seafloor sediments by inversion of precritical reflection data," *IEEE J. Oceanic Eng.*, vol. 13, pp. 215–221, 1988.
- [42] E. Michelozzi, P. Guerrini, R. Chiarabini, B. Tonarelli, and M. C. Mori, "Yellow Shark core data analysis," SACLANT Undersea Res. Centre, La Spezia, Italy, 1996, SACLANTCEN unpublished document.
- [43] T. Akal, C. Gehin, B. Matteucci, and B. Tonarelli, "Measured and computed physical properties of sediment cores, Island of Elba zone," SACLANT Undersea Res. Centre, La Spezia, Italy, 1972, SACLANTCEN document M-82.
- [44] E. L. Hamilton, "Compressional-wave attenuation in marine sediments," *Geophysics*, vol. 37, no. 4, pp. 620–646, 1972.
- [45] ———, "Geoacoustic modeling of the seafloor," *J. Acoust. Soc. Amer.*, vol. 68, no. 5, pp. 1313–1340, 1980.
- [46] F. B. Jensen, "Comparison of transmission loss data for different shallow-water areas with theoretical results provided by a three-fluid normal-mode propagation model," in *Sound Propagation in Shallow Water*, vol. II, O. F. Hastrup and O. V. Oleson, Eds., SACLANT Undersea Res. Centre, La Spezia, Italy, 1974, SACLANTCEN document CP-14, pp. 79–92.
- [47] O. F. Hastrup, "Some bottom-reflection loss anomalies near grazing and their effect on propagation in shallow water," in *Bottom-Interacting*

- Ocean Acoustics*, W. Kuperman and F. Jensen, Eds. New York: Plenum, 1980, pp. 135–152.
- [48] D. J. Thompson, "Jackknifing using multiple-window spectra," in *Proc. IEEE ICASSP '94*, 1995, pp. 73–76.
- [49] C. F. Mecklenbräuer, D. Maiwald, and J. F. Böhme, "F-Test in matched field processing: Identifying multimode propagation," in *Proc. IEEE ICASSP '95*, 1995, pp. 3123–3126.
- [50] F. B. Jensen and M. C. Ferla, "SNAP—The SACLANTCEN normal mode acoustic propagation model," SACLANT Undersea Res. Centre, La Spezia, Italy, 1979, SACLANTCEN document SM-121.
- [51] P. Gerstoft, "Inversion of acoustic data using a combination of genetic algorithms and the Gauss–Newton approach," *J. Acoust. Soc. Amer.*, vol. 97, no. 4, pp. 2181–2190, 1995.
- [52] ———, "SAGA: Seismo-acoustic inversion using genetic algorithms," SACLANTCEN unpublished document, 1996.



**Jean-Pierre Hermand** received the Ingénieur Civil and Ph.D. degrees in electrical and telecommunication engineering from the University of Brussels (ULB).

He joined the SACLANT Undersea Research Centre, La Spezia, Italy, in 1985, as a scientist where he has been engaged in research for various projects involving underwater acoustics and magnetics. From 1991 to 1993, he was a consultant to the Naval Undersea Warfare Center (NUWC) on broad-band environmentally-adaptive signal processing for active sonar application. Since 1991, he has been a lecturer of a course in image processing at the International School of Optical Technologies (AILUN), Italy. He is now project leader with SACLANTCEN leading research activities on broad-band tomographic measurement techniques and inversion methodologies for shallow water and coastal environments.



**Peter Gerstoft** received the M.Sc. degree from both the Technical University of Denmark in 1983 and from University of Western Ontario, in 1984, and the Ph.D. degree from the Technical University of Denmark in 1986. From 1987 to 1992, he was employed at Ødegaard and Dannekiold-Samsøe in Denmark working on forward modeling for seismic exploration, and from 1989 to 1990, he was Visiting Scientist at Massachusetts Institute of Technology and at Woods Hole Oceanographic Institute. Since 1992, he has been a Senior Scientist at SACLANT Undersea Research Centre, Italy. His research interests include global optimization, modeling and inversion of acoustic signals. He is a member of Society of Exploration Geophysics and Acoustical Society of America.